

A New Approach to Compositional Data Analysis using L^∞ -normalization with Applications to Vaginal Microbiome

Pawel Gajer*¹ and Jacques Ravel¹

¹Center for Advanced Microbiome Research and Innovation (CAMRI), Institute for Genome Sciences, and Department of Microbiology and Immunology, University of Maryland School of Medicine

March 28, 2025

Abstract

This paper introduces a novel approach to compositional data analysis based on L^∞ -normalization, addressing the challenges posed by zero-rich high-throughput compositional data such as microbiome datasets. Traditional methods like Aitchison's logistic transformations require excluding zeros, which conflicts with the reality that most high-throughput omics datasets contain structural zeros that cannot be removed without violating the inherent structure of the system. Moreover, such datasets exist exclusively on the boundary of compositional space, making traditional interior-focused approaches fundamentally misaligned with the data's true nature.

We present a family of L^p -normalizations, focusing primarily on L^∞ -normalization due to its advantageous properties. This approach identifies the compositional space with the L^∞ -simplex, which can be represented as a union of top-dimensional faces called L^∞ -cells. Each L^∞ -cell consists of samples where one component's absolute abundance equals or exceeds all others, and carries a coordinate system identifying it with a d-dimensional unit cube.

When applied to vaginal microbiome data, the L^∞ -decomposition method aligns well with established Community State Type (CST) classifications while offering several advantages: (1) each L^∞ -CST is named after its dominating component, (2) L^∞ -decomposition has clear biological meaning, (3) it remains stable under addition or subtraction of samples, (4) it resolves issues associated with cluster-based approaches, and (5) each L^∞ -cell provides a homogeneous coordinate system for exploring internal structure.

Furthermore, we extend homogeneous coordinates to the entire sample space through a cube embedding technique, mapping compositional data into a d-dimensional unit cube. These various cube embeddings can be integrated through their Cartesian product, providing a unified representation of compositional data from multiple perspectives. While demonstrated through microbiome studies, these methods are applicable to any compositional data type.

Keywords: Compositional data analysis, Community State Types (CSTs), Vaginal microbiome, Zero-rich data, Subcompositional coherence, Projective geometry

*Research reported in this publication was supported by grant number INV-048956 from the Gates Foundation.

1. Introduction

The advent of high-throughput techniques, generating mainly compositional data, has introduced unique analytical challenges. Aitchison’s groundwork in compositional data analysis, which proposed logistic transformations necessitating exclusion of zeros [1, 2], contrasts starkly with the zero-rich nature of high-throughput compositional data. From a geometric viewpoint, assuming data has no zeros implies that it resides entirely within the interior of the compositional space. However, in reality, most high-throughput omics datasets exist solely on the boundary of the compositional space, with not a single data point located in the space’s interior. To address this issue, researchers have turned to methods such as missing-data imputation or the addition of pseudo-counts to eliminate zeros, effectively shifting the data from the compositional space’s boundary to its interior. These adjustments have a considerable impact on the outcomes of subsequent analyses, especially considering the prevalence of zeros in most high-throughput datasets. Despite the significance of these changes, conducting sensitivity analyses to evaluate their effects is remarkably neglected.

To address the challenges posed by zeros in compositional data, we introduce a family of L^p -normalizations, with p representing either a positive real number or infinity. The Total Sum Scaling (division of the rows of a data matrix by the total row sums), used routinely to normalize compositional data, is a special case of the family of transformations corresponding to $p = 1$. Our focus, however, is primarily on L^∞ -normalization due to its advantageous properties.

L^∞ -normalization identifies the compositional space with the L^∞ -simplex, which can be represented as a union of its top-dimensional faces, called L^∞ -cells (see Figure 1). The k -th cell consists of samples where the absolute abundance of the k -th component is equal to or greater than the absolute abundances of all other components. For example, in the context of shotgun metagenomic data, the k -th component consists of samples where the abundance of the k -th gene is greater than or equal to the abundance of any other genes. Moreover, each cell carries a coordinate system identifying it with the d -dimensional unit cube $[0, 1]^d$, where d is the dimensionality of the compositional space equal to the number of components minus one. Although high-throughput datasets might feature a large number of components, corresponding to different types of biomarkers, and consequently, L^∞ -cells, the count of L^∞ -cells that actually hold data tends to be notably small.

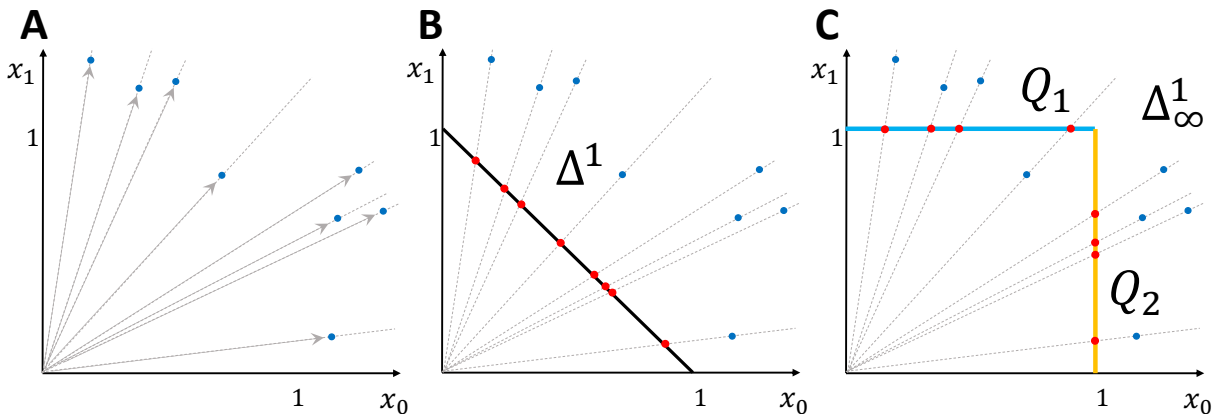


Figure 1: Compositional data reflects relative proportions, not absolute values. A compositional measurement vector (an arrow with a blue disk at the end in panel A) represents any point along the dashed line, as they share the same proportions. This leads to multiple ways to represent the compositional space as a hypersurface. Panel B shows the standard simplex (Δ^1) representation of 1D compositional space, while panel C shows the L^∞ -simplex (Δ_∞^1) representation, together with its two top dimensional faces (L^∞ -cells): Q_1 in blue and Q_2 in orange. The faces Q_1 and Q_2 can be identified with the unit interval $[0, 1]$. In higher dimensions, each L^∞ -cell can be identified with a cube $[0, 1]^d$, where d is the dimensionality of the compositional space equal to the number of components minus one.

In studies involving human vaginal microbiome, analyzing unique DNA sequence variations — known as Amplicon Sequence Variants (ASVs) — using the L^∞ -decomposition method aligns well with established methods for categorizing vaginal microbial communities into different community types. This suggests that L^∞ -decomposition could be a viable alternative method for high-level characterization of these and other bacterial communities as well as other compositional data types.

Since, from the perspective of downstream analyses it is practical to focus on L^∞ -cells with a substantial number of data samples, we define truncated L^∞ -decomposition for the compositional data, reassigning samples from less populated L^∞ -cells to those with adequate number of samples. This rearrangement is supported by the observation that samples in lesser-populated L^∞ -cells are typically situated near the boundary of that cell adjoining L^∞ -cells with a high sample count. In this context, we refer to the cells of truncated L^∞ -decomposition as L^∞ -CSTs, providing a new perspective on community state classifications.

L^∞ -CSTs have several advantages over the classical CSTs or enterotypes (in the context of gut microbiome): 1) The name of each L^∞ -CST is the name of the component that dominates (at the absolute abundance) the corresponding set of samples, 2) the definition of L^∞ -CST has a simple and easy to understand biological meaning, 3) L^∞ -decomposition is stable under addition or subtraction of samples - that is the membership of a sample in a given L^∞ -cell is not dependent on other samples, 4) L^∞ -cells are not clusters, but absolute abundances dominance patterns of the components of the data - resolving all issues associated with the construction of CSTs or enterotypes as clusters (see Section 6 for more details), 5) L^∞ -cell is not only a grouping of samples, but each L^∞ -cell comes with a homogeneous coordinate system that allows further elucidation of the internal structure of that cell. This projective geometry coordinate system, introduced by August Ferdinand Möbius in 1827, corresponds to Cartesian coordinates in Euclidean geometry [8]. The log-transform of homogeneous coordinates is the Aitchison’s additive log ratio transform.

Utilizing elementary geometro-topological ideas, we have extended homogeneous coordinates from a subset of samples, where the denominator of the transformation is non-zero, to the entire sample space. This expansion results in a new parametrization of the compositional data, which we refer to as a cube embedding, that maps the data into a d -dimensional cube $[0, 1]^d$, where d is the number of components of the compositional data minus one.

Cube embeddings result in a variety of compositional data representations, providing insights into the data’s structure from multiple perspectives. Similar to how varying angles of tomographic imaging are employed to piece together the three-dimensional structure of internal organs, or how different maps of the Earth facilitate analysis of different geo-spacial phenomena, this technique facilitates a more comprehensive understanding of compositional data’s structure. However, the abundance of representations introduces complexity, prompting the question: Can these diverse representations be integrated? A unified representation of the data can be taken to be the Cartesian product of the cube embeddings associated with L^∞ -CSTs. This approach is detailed in Section 10.

The emphasis in the paper is on compositional data in the context of microbiome studies. Yet, all methods can be applied in the context of any type of compositional data.

The paper is organized as follows: Section 2 introduces the concept of compositional spaces and their properties. Section 3 discusses subcompositional coherence and its relevance to omics data. Section 4 explores various parametrizations of compositional spaces, focusing on L^p -normalizations. Section 5 presents the L^∞ -decomposition of compositional spaces into L^∞ -cells. Section 6 compares VALENCIA Community State Types (CSTs) with L^∞ -CSTs, illustrating the advantages of the latter. Section 7 describes the alignment of L^∞ -cells through rotation to create a global coordinate system. Section 8 introduces hypercube embeddings of compositional data, extending homogeneous coordinates to the entire sample space. Section 9 demonstrates the integration of cube embeddings to provide a unified representation of the data. Section 10 concludes with a discussion of the implications and potential applications of the presented methods.

2. Compositional Spaces

Most omics data types, such as 16S rRNA and metagenomic, exhibit an asymptotically compositional nature. This means that for two read count sets $x = (x_0, x_1, \dots, x_d)$ and $x' = (x'_0, x'_1, \dots, x'_d)$ from the same sample, with total read counts $T(x)$ and $T(x')$ respectively, as the total read counts $T(x)$ and $T(x')$ increase, the proportions $\frac{x}{T(x)}$ and $\frac{x'}{T(x')}$ become closer and closer to each other. That is

$$\lim_{\min(T(x), T(x')) \rightarrow \infty} \left\| \frac{x}{T(x)} - \frac{x'}{T(x')} \right\| = 0.$$

The deviations from exact proportionality can be attributed to sampling errors and, more significantly, the presence of zero components due to detection limits.

In practical applications, it is assumed that the data is compositional, meaning that a vector representing proportions of different components in a sample is defined up to a positive scaling factor. Since all components, x_i , of a compositional vector $x = (x_0, x_1, \dots, x_d)$ are non-negative and the vector cannot be zero, it can be identified with a point of $\mathbb{R}_{\geq 0}^{d+1} - \{0\}$. In this context, any compositional vector x represents a class of equivalent vectors:

$$[x] = \{\lambda x : x \in \mathbb{R}_{\geq 0}^{d+1} - \{0\}, \lambda > 0\}$$

derived from scaling x by various factors. The equivalence class of a point (x_0, x_1, \dots, x_d) is denoted as $[x_0 : x_1 : \dots : x_d]$. Geometrically, $[x]$ represents the line passing through the origin in $\mathbb{R}_{\geq 0}^{d+1}$ spanned by x as illustrated in Figure 2.

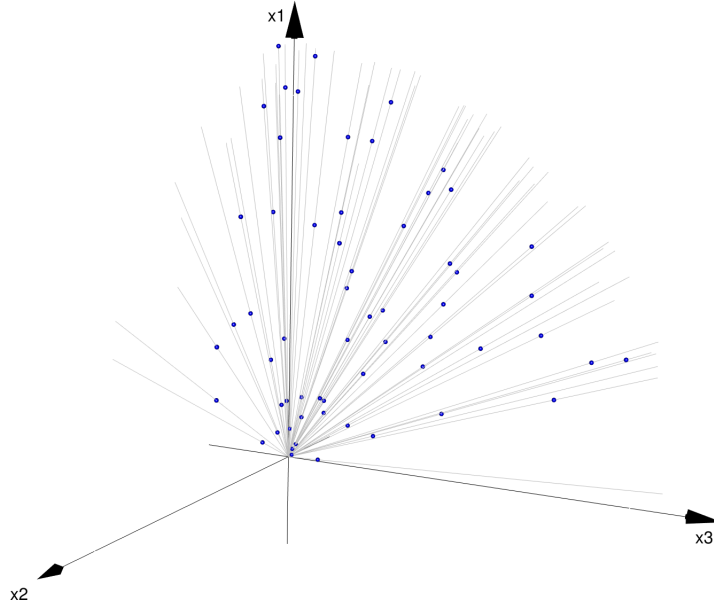


Figure 2: Random sample of points of $\mathbb{RP}_{\geq 0}^2$ represented by lines through the origin with representatives that determine these lines marked with blue spheres.

The space $\mathbb{RP}_{\geq 0}^d$ of lines through the origin in $\mathbb{R}_{\geq 0}^{d+1}$, hereafter referred to as the d -dimensional *compositional space*, is a subset of a *real projective space* \mathbb{RP}^d defined as a space of lines through the origin in \mathbb{R}^{d+1} . Since every line through the origin in \mathbb{R}^{d+1} intersects the unit sphere S^d in exactly two antipodal points, \mathbb{RP}^d can be identified with the quotient space of the sphere S^d with every pair of antipodal points collapsed to a single point. Real projective space is a fundamental example of a non-trivial smooth manifold [10, 6]. That is, there does not exist a global coordinate system on \mathbb{RP}^d that would identify that space with \mathbb{R}^d . Instead, \mathbb{RP}^d is equipped with an atlas of charts, $\{\phi_\alpha : U_\alpha \rightarrow \mathbb{R}^d\}_{\alpha \in I}$, such that every point of \mathbb{RP}^d belongs to at

least one U_α and if $U_\alpha \cap U_\beta \neq \emptyset$, then the composition $\phi_\alpha \circ \phi_\beta^{-1} : \mathbb{R}^d \rightarrow \mathbb{R}^d$ is a diffeomorphism, which means that it is a smooth map whose inverse is also smooth [6]. The standard atlas of \mathbb{RP}^d consists of homogeneous coordinate charts. The i -th homogeneous coordinate chart is a map $\phi_i : U_i = \mathbb{RP}^d - \{x_i = 0\} \rightarrow \mathbb{R}^d$ defined as

$$\phi_i([x_0 : x_1 : \dots : x_d]) = \left(\frac{x_0}{x_i}, \dots, \frac{x_{i-1}}{x_i}, 1, \frac{x_{i+1}}{x_i}, \dots, \frac{x_d}{x_i} \right)$$

where $\{x_i = 0\}$ is a subset of \mathbb{RP}^d consisting of points $[x_0 : x_1 : \dots : x_d]$ of such that $x_i = 0$. Thus, each point in $\{x_i = 0\}$ corresponds to a line in \mathbb{R}^{d+1} contained in the hyperplane $x_i = 0$. Geometrically, the map ϕ_i assigns to the line $[x]$, span by a vector $x \in \mathbb{R}^{d+1} - \{0\}$, the point of intersection of $[x]$ with the hyperplane $x_i = 1$. Going forward, the notation ϕ_i will also refer to the restriction of this map to the compositional space $\mathbb{RP}_{\geq 0}^d \subset \mathbb{RP}^d$.

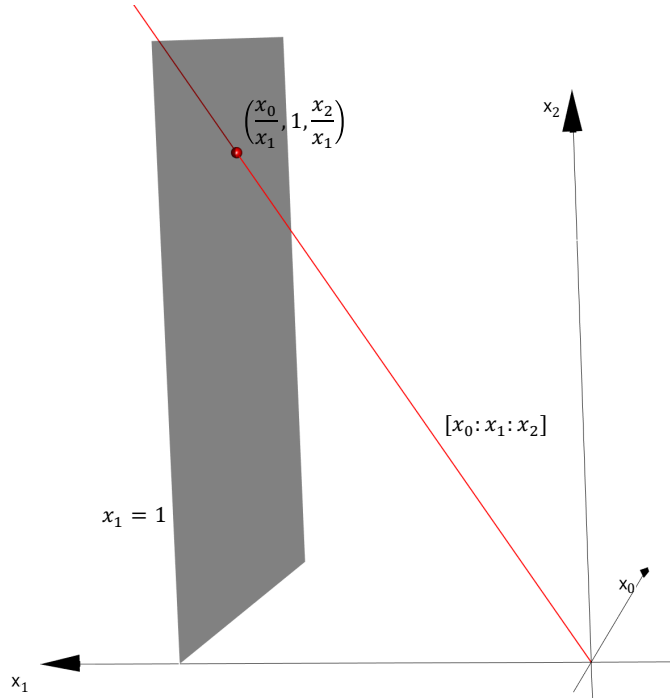


Figure 3: Geometric interpretation of the x_1 -homogeneous coordinate chart ϕ_1 as a map that assigns to the line $\{\lambda(x_0, x_1, x_2)\}$, shown in red, representing a point $[x_0 : x_1 : x_2]$ of \mathbb{RP}^d , the intersection $(\frac{x_0}{x_1}, 1, \frac{x_2}{x_1})$ of the line with the plane $x_1 = 1$.

A function $f : \mathbb{RP}_{\geq 0}^d \rightarrow \mathbb{R}$ over a compositional space $\mathbb{RP}_{\geq 0}^d$ assigns a unique real number $f([x])$ to each point $[x]$ within $\mathbb{RP}_{\geq 0}^d$. Since, $\mathbb{RP}_{\geq 0}^d$ is a quotient of $\mathbb{R}_{\geq 0}^{d+1} - \{0\}$, and we typically use representatives (x_0, x_1, \dots, x_d) of points in $\mathbb{RP}_{\geq 0}^d$ in practical applications, it's important to characterize a function over $\mathbb{RP}_{\geq 0}^d$ in terms of $\mathbb{R}_{\geq 0}^{d+1} - \{0\}$. A function $f : \mathbb{R}_{\geq 0}^{d+1} - \{0\} \rightarrow \mathbb{R}$ induces a function over $\mathbb{RP}_{\geq 0}^d$ if it is scale invariant, which means that $f(x) = f(\lambda x)$ holds true for all x in $\mathbb{R}_{\geq 0}^{d+1} - \{0\}$ and any positive value of λ .

Example 2-A: Let $d : \mathbb{RP}_{\geq 0}^d \times \mathbb{RP}_{\geq 0}^d \rightarrow [0, \infty)$ be a metric over $\mathbb{RP}_{\geq 0}^d$, then for any point x_{ref} of $\mathbb{RP}_{\geq 0}^d$, the distance to x_{ref} , $f(x) = d(x, x_{\text{ref}})$, is a function over $\mathbb{RP}_{\geq 0}^d$.

Example 2-B: The angular distance

$$d_{\text{angle}}([x_0 : \dots : x_d], [y_0 : \dots : y_d]) = \cos^{-1} (\langle \pi_1([x_0 : \dots : x_d]), \pi_1([y_0 : \dots : y_d]) \rangle)$$

where

$$\pi_1([x_0 : \dots : x_d]) = \frac{(x_0, \dots, x_d)}{\|(x_0, \dots, x_d)\|_1}$$

assigns to each line $\{\lambda(x_0, \dots, x_d)\}_{\lambda \in [0, \infty)}$ representing $[x_0 : \dots : x_d]$, the unit vector on that line. The inner product between two unit vectors is the cosine of the angle between them. Thus, the angular distance between two points of $\mathbb{RP}_{\geq 0}^d$ is the angle between the associated unit vectors.

The angular distance is an example of a construct of a metric on $\mathbb{RP}_{\geq 0}^d$ that is induced by a metric on a particular parametrization of $\mathbb{RP}_{\geq 0}^d$. In the case of angular distance it is an L^2 or spherical parametrization of $\mathbb{RP}_{\geq 0}^d$. Different parametrizations of compositional spaces will be discussed in more detail in Section 3. Thus, even if a dissimilarity measure is not well defined on a compositional space, any parametrization of a compositional space can be used to extend the dissimilarity measure from the parametrization to the compositional space. For example, Bray-Curtis dissimilarity d_{BC} is not well defined on $\mathbb{RP}_{\geq 0}^d \times \mathbb{RP}_{\geq 0}^d$, as it is not homogeneous, meaning $d_{\text{BC}}(\lambda_0 x, \lambda_1 y) = d_{\text{BC}}(x, y)$ is not true for d_{BC} for any $\lambda_0, \lambda_1 > 0$. Yet, the restriction of d_{BC} to a particular parametrization π of $\mathbb{RP}_{\geq 0}^d$ defines a dissimilarity measure on $\mathbb{RP}_{\geq 0}^d$:

$$d_{\text{BC}}([x], [y]) := d_{\text{BC}}(\pi([x]), \pi([y])).$$

Example 2-C: The ratio of any two components $[x_0 : x_1 : \dots : x_d] \mapsto \frac{x_j}{x_i}$ is a function $\phi_{ji} : \mathbb{RP}_{\geq 0}^d - \{x_i = 0\} \rightarrow [0, \infty)$ over $\mathbb{RP}_{\geq 0}^d - \{x_i = 0\}$, where $\{x_i = 0\}$ is a subset of points $[x_0 : x_1 : \dots : x_d]$ of $\mathbb{RP}_{\geq 0}^d$ with $x_i = 0$, as for any representative $(\lambda x_0, \lambda x_1, \dots, \lambda x_d)$ of $[x_0 : x_1 : \dots : x_d]$, we have $\frac{\lambda x_j}{\lambda x_i} = \frac{x_j}{x_i}$.

Example 2-D: In the one-dimensional case, the function $\phi_1 : \mathbb{RP}_{\geq 0}^1 - \{x_1 = 0\} \rightarrow [0, \infty)$ is defined by $\phi_1([x_0 : x_1]) = \frac{x_0}{x_1}$. ϕ_1 extends to a function $\hat{\phi}_1 : \mathbb{RP}_{\geq 0}^1 \rightarrow [0, \infty)^*$, where $\hat{\phi}_1([1 : 0]) = \infty$, and $[0, \infty)^*$ is a one-point compactification of $[0, \infty)$, that adds a point ∞ to the original interval with the open intervals (a, ∞) forming open neighborhoods of ∞ in $[0, \infty)^*$ [7]. This compactified space $[0, \infty)^*$ is homeomorphic to the interval $[0, 1]$. That is, it is continuous and has an inverse that is also continuous [7]. In fact, any continuous and monotonically increasing function $\sigma : [0, \infty) \rightarrow [0, 1]$ that approaches 1 as x approaches infinity, induces a homeomorphism between $[0, \infty)^*$ and $[0, 1]$ if extended by setting $\sigma(\infty) = 1$. For example, we can take σ to be $\sigma(x) = 1 - e^{-\lambda x}$ for any $\lambda > 0$.

Similarly, a function $\phi_1^\sigma = \sigma \circ \phi_1 : \mathbb{RP}_{\geq 0}^1 - \{x_1 = 0\} \rightarrow [0, 1]$ defined as $\phi_1^\sigma([x_0 : x_1]) = \sigma\left(\frac{x_0}{x_1}\right)$, extends to a function $\hat{\phi}_1^\sigma : \mathbb{RP}_{\geq 0}^1 \rightarrow [0, 1]$, where $\hat{\phi}_1^\sigma([1 : 0]) = 1$. This extension is a homeomorphism between $\mathbb{RP}_{\geq 0}^1$ and the unit interval $[0, 1]$. Later in this section, we will explore a higher-dimensional generalization of this function that allows for the parametrization of $\mathbb{RP}_{\geq 0}^d$ via the unit hyper-cube $[0, 1]^d$.

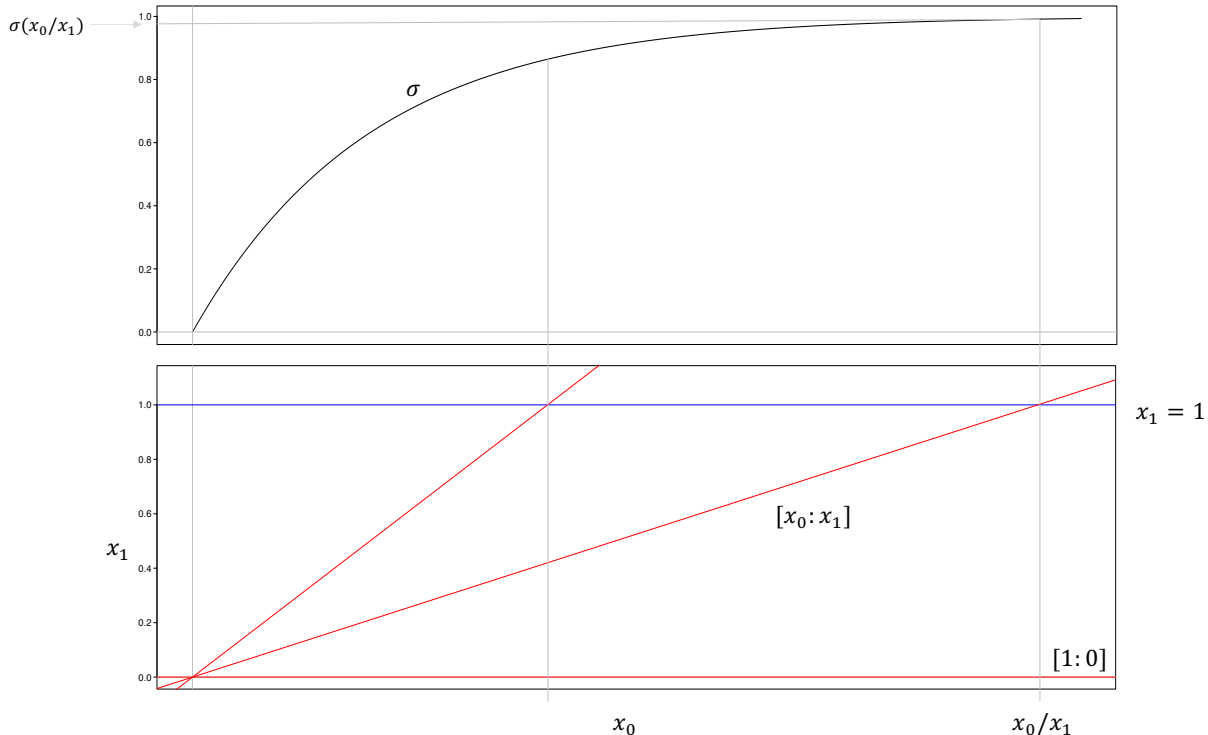


Figure 4: Extension of ϕ_1^σ to $\mathbb{RP}_{\geq 0}^1$. Each red line in the plot of the lower panel corresponds to a point of $\mathbb{RP}_{\geq 0}^1 - \{x_1 = 0\}$. The x -coordinate of the intersection of each of the red lines with the blue line of $x_1 = 1$, is the geometric interpretation of the map ϕ_1 . The vertical gray lines indicate the values of ϕ_1 at the corresponding points of $\mathbb{RP}_{\geq 0}^1 - \{x_1 = 0\}$. As the point (red line) $[x_0 : x_1]$ of $\mathbb{RP}_{\geq 0}^1 - \{x_1 = 0\}$ gets closer and closer to the line $x_1 = 0$, corresponding to the point $[1 : 0]$ of $\mathbb{RP}_{\geq 0}^1$, the value of σ at $\phi_1([x_0 : x_1])$ gets closer and closer to 1. Thus, setting $\phi_1^\sigma([1 : 0]) = 1$ extends ϕ_1^σ to a mapping identifying $\mathbb{RP}_{\geq 0}^1$ with $[0, 1]$.

Example 2-E: The i -th coordinate x_i of a point $[x_0 : x_1 : \dots : x_d]$ is not a function over the compositional space $\mathbb{RP}_{\geq 0}^d$ as for two different representations (x_0, x_1, \dots, x_d) and $(\lambda x_0, \lambda x_1, \dots, \lambda x_d)$ of $[x_0 : x_1 : \dots : x_d]$, i -th coordinates x_i and λx_i of these representations have distinct values for $\lambda \neq 1$. Thus, if we take $\mathbb{RP}_{\geq 0}^d$ to be a sample space, the i -th coordinate assignment $[x_0 : x_1 : \dots : x_d] \mapsto x_i$ is not random variable over $\mathbb{RP}_{\geq 0}^d$.

The notion of a function over $\mathbb{RP}_{\geq 0}^d$ extends to the notion of a mapping $f : \mathbb{RP}_{\geq 0}^d \rightarrow X$ from $\mathbb{RP}_{\geq 0}^d$ to any topological space X . Such mapping assigns exactly one value to every point $[x]$ of $\mathbb{RP}_{\geq 0}^d$. Similarly, as in the function case, a mapping $f : \mathbb{R}_{\geq 0}^{d+1} - \{0\} \rightarrow X$ induces a mapping $f' : \mathbb{RP}_{\geq 0}^d \rightarrow X$ if f is scale invariant. A mapping $f : \mathbb{RP}_{\geq 0}^d \rightarrow X$ is a parametrization of $\mathbb{RP}_{\geq 0}^d$ if it is a homeomorphism. We will explore different parametrizations of $\mathbb{RP}_{\geq 0}^d$ in Section 4.

3. Subcompositional Coherence

Compositional data in omics studies, such as those found in 16S rRNA amplicon, metabolomics, and metagenomics, inherently include only a subset of all possible components. This subcompositional nature arises because some microbes may be present at levels below detectable thresholds and thus remain undetected and omitted from the dataset, despite their actual presence. This selective exclusion of components based on detectability skews the relative abundances of those detected. It is crucial for data analysis methods to acknowledge and directly address this subcompositional character of the data.

In the context of omics data, component sub-sampling is not random but inherently selective, focusing predominantly on the most reliably detectable components. This aspect challenges the traditional definition of subcompositional coherence, which demands that analytical methods yield consistent results, irrespective of whether they are applied to the entire set of components or just a subset. Traditionally, subcompositional coherence is defined as the invariance of a procedure or transformation with respect to an arbitrary operation of subsetting components. More formally, a family of maps $\{f^d : U^d \rightarrow \mathbb{R}^{n(d)}\}_{d>0}$, where $n(d)$ is a positive integer function of d and U^d is a subset of $\mathbb{RP}_{\geq 0}^d$, is considered subcompositionally coherent if for any component sub-setting operation π , there exists a corresponding map π' that maintains the coherence as illustrated by the following commutative diagram:

$$\begin{array}{ccc} U^d & \xrightarrow{f^d} & \mathbb{R}^{n(d)} \\ \pi \downarrow & & \downarrow \pi' \\ U^m & \xrightarrow{f^m} & \mathbb{R}^{n(m)} \end{array}$$

However, this standard definition of subcompositional coherence requires the procedure or transformation to be invariant with respect to any sub-sampling of components operation, which may be overly stringent for omics data. In the context of omics studies, a more appropriate criterion for subcompositional coherence would be to maintain consistency when sub-sampling eliminates components of low abundance. Therefore, for compositional omics data, a transformation or procedure might only need to maintain consistency when less abundant components are eliminated. This modified version of subcompositional coherence, tailored to the selective nature of omics data sub-sampling, ensures that the analytical methods yield consistent results when applied to either the full compositional data or a subset of its components, focusing on the most reliably detectable components.

Example 3-A: The first component ratio charts $\{\phi_0^d : \mathbb{RP}_{\geq 0}^d - \{x_0 = 0\} \rightarrow \mathbb{R}^d\}$

$$\phi_0^d([x_0 : x_1 : x_2 : \dots : x_d]) = \left(\frac{x_1}{x_0}, \frac{x_2}{x_0}, \dots, \frac{x_d}{x_0} \right)$$

are subcompositionally coherent with respect to an arbitrary subsetting operation as restriction of ϕ_0^d to any subset of $(m + 1)$ components (that does not include x_0) gives the map ϕ_0^m . For example, for $d = 5$

$$\phi_0^4([x_0 : x_1 : x_2 : x_3 : x_4]) = \left(\frac{x_1}{x_0}, \frac{x_2}{x_0}, \frac{x_3}{x_0}, \frac{x_4}{x_0} \right)$$

is invariant with respect to the subset selection of the first three components as then ϕ_0^5 becomes ϕ_0^3

$$\phi_0^3([x_0 : x_1 : x_2]) = \left(\frac{x_1}{x_0}, \frac{x_2}{x_0} \right)$$

Thus, $\pi' \circ \phi_0^4 = \phi_0^3 \circ \pi$ for π the sub-setting of the first three components and $\pi' : \mathbb{R}^4 \rightarrow \mathbb{R}^2$ the projection on the first two components $\pi'(r_0, r_1, r_2, r_3) = (r_0, r_1)$.

Example 3-B: The centered ratio transformations $\{\psi^d : \mathbb{RP}_{\geq 0}^d - \{\prod_{i=0}^d x_i = 0\} \rightarrow \mathbb{R}^d\}$

$$\psi^d([x_0 : x_1 : \dots : x_d]) = \left(\frac{x_0}{(\prod_{i=0}^d x_i)^{1/(d+1)}}, \frac{x_1}{(\prod_{i=0}^d x_i)^{1/(d+1)}}, \dots, \frac{x_d}{(\prod_{i=0}^d x_i)^{1/(d+1)}} \right)$$

are not subcompositionally coherent. For example, for $d = 5$

$$\psi^4([x_0 : x_1 : x_2 : x_3 : x_4]) = \left(\frac{x_0}{(\prod_{i=0}^4 x_i)^{1/5}}, \frac{x_1}{(\prod_{i=0}^4 x_i)^{1/5}}, \frac{x_2}{(\prod_{i=0}^4 x_i)^{1/5}}, \frac{x_3}{(\prod_{i=0}^4 x_i)^{1/5}}, \frac{x_4}{(\prod_{i=0}^4 x_i)^{1/5}} \right)$$

and if we restrict ψ^4 to the first three components, we will not get ψ^2

$$\psi^2([x_0 : x_1 : x_2]) = \left(\frac{x_0}{(\prod_{i=0}^2 x_i)^{1/3}}, \frac{x_1}{(\prod_{i=0}^2 x_i)^{1/3}}, \frac{x_2}{(\prod_{i=0}^2 x_i)^{1/3}} \right)$$

as in general $\frac{x_i}{(x_0 x_1 x_2)^{1/3}}$ is not equal to $\frac{x_i}{(x_0 x_1 x_2 x_3 x_4)^{1/5}}$. Thus, the centered log ratio is not invariant with respect to the component sub-setting operation. This implies that the centered log ratio transformations are also not subcompositionally coherent.

4. Parametrizations of Compositional Spaces

There are infinite number of parametrizations of $\mathbb{RP}_{\geq 0}^d$. Indeed, any d -dimensional smooth hypersurface H in \mathbb{R}^{d+1} with the property that each line, representing a point of $\mathbb{RP}_{\geq 0}^d$, intersects H at exactly one point, induces a parametrization of $\mathbb{RP}_{\geq 0}^d$. For example, if we take H to be the unit d -dimensional sphere S^d , we get a homeomorphism between $\mathbb{RP}_{\geq 0}^d$ and the L^2 -simplex

$$\Delta_2^d = S^d \cap \mathbb{R}_{\geq 0}^{d+1} = \{x \in \mathbb{R}_{\geq 0}^{d+1} : \|x\|_2 = 1\}$$

where $\|x\|_2 = (\sum_{i=0}^d |x_i|^2)^{1/2}$ is the L^2 -norm of x . The projection on the unit sphere $\pi_1 : \mathbb{R}_{\geq 0}^{d+1} - \{0\} \rightarrow \Delta_2^d$ defined by $\pi_1(x) = \frac{x}{\|x\|_2}$ is called the L^2 -normalization of the compositional data.

Similarly, any L^p -norm, $p \geq 1$ or $p = \infty$, or L^p -quasi-norm, where $0 < p < 1$, induces a parametrization of $\mathbb{RP}_{\geq 0}^d$ with the corresponding L^p -normalization given by the projection $\pi_p : \mathbb{R}_{\geq 0}^{d+1} - \{0\} \rightarrow \Delta_p^d$, where Δ_p^d is the L^p -simplex

$$\Delta_p^d = \{x \in \mathbb{R}_{\geq 0}^{d+1} : \|x\|_p = 1\}$$

where $\pi_p(x) = \frac{x}{\|x\|_p}$ with $\|x\|_p = (\sum_{i=0}^d |x_i|^p)^{1/p}$ for $p > 0$ and $\|x\|_\infty = \max_i |x_i|$. In particular, for $p = 1$, the standard simplex Δ^d is the intersection of the L^1 unit sphere

$$S_1^d = \{x \in \mathbb{R}^{d+1} : \|x\|_1 = 1\}$$

and the positive orthant $\mathbb{R}_{\geq 0}^{d+1}$.

The following figures show 1d and 2d unit L^p -spheres with the corresponding L^p simplices (in red).

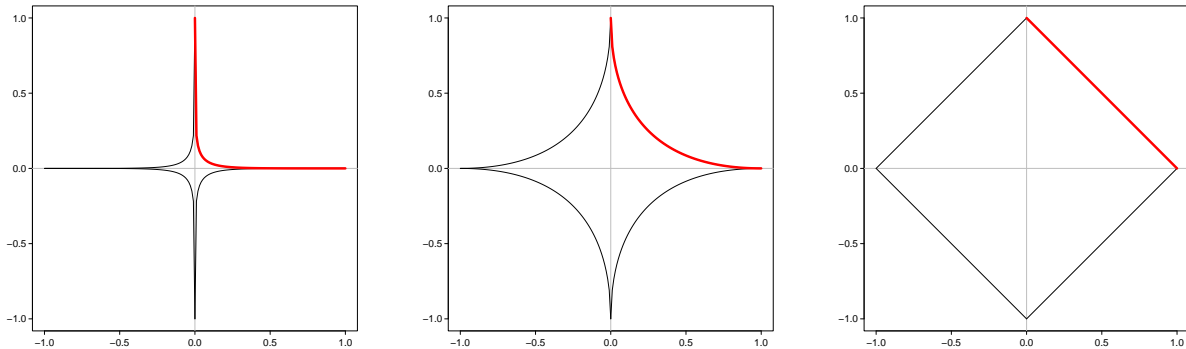


Figure 5: One dimensional unit L^p -spheres with the corresponding L^p simplices for $p = 0.25$ (left) $p = 0.5$ (middle) and $p = 1$ (right).

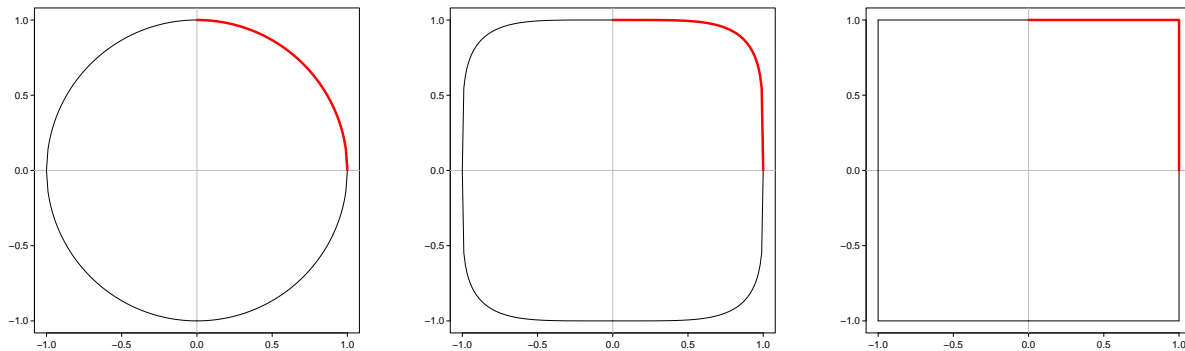


Figure 6: One dimensional unit L^p -spheres with the corresponding L^p simplices for $p = 2$ (left) $p = 5$ (middle) and $p = \infty$ (right).

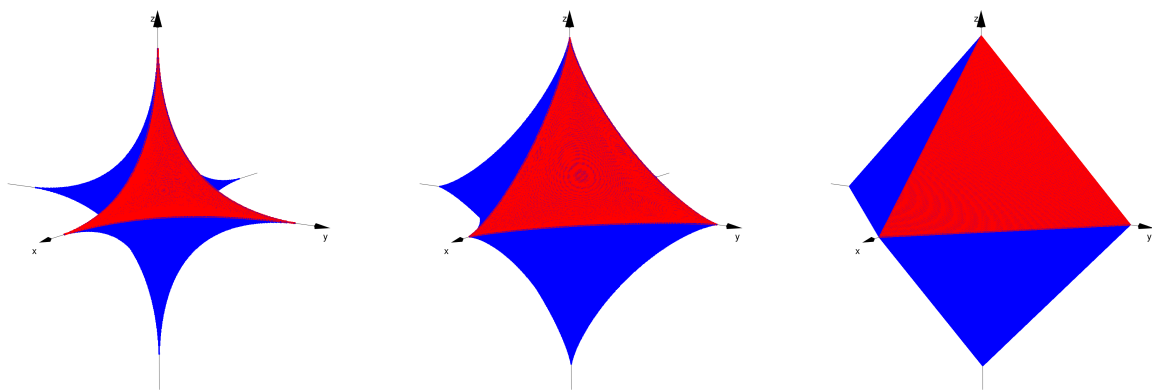


Figure 7: Two dimensional unit L^p -spheres with the corresponding L^p simplices for $p = 0.25$ (left) $p = 0.5$ (middle) and $p = 1$ (right).

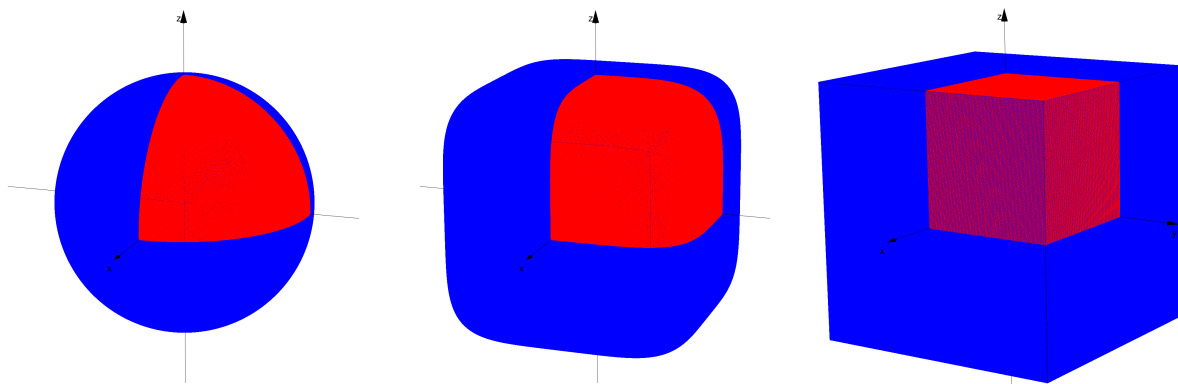


Figure 8: Two dimensional unit L^p -spheres with the corresponding L^p simplices for $p = 2$ (left) $p = 5$ (middle) and $p = \infty$ (right).

Figure 9 illustrates the process of L^1 and L^∞ -normalization on the compositional data shown in Figure 2 of Section 2.

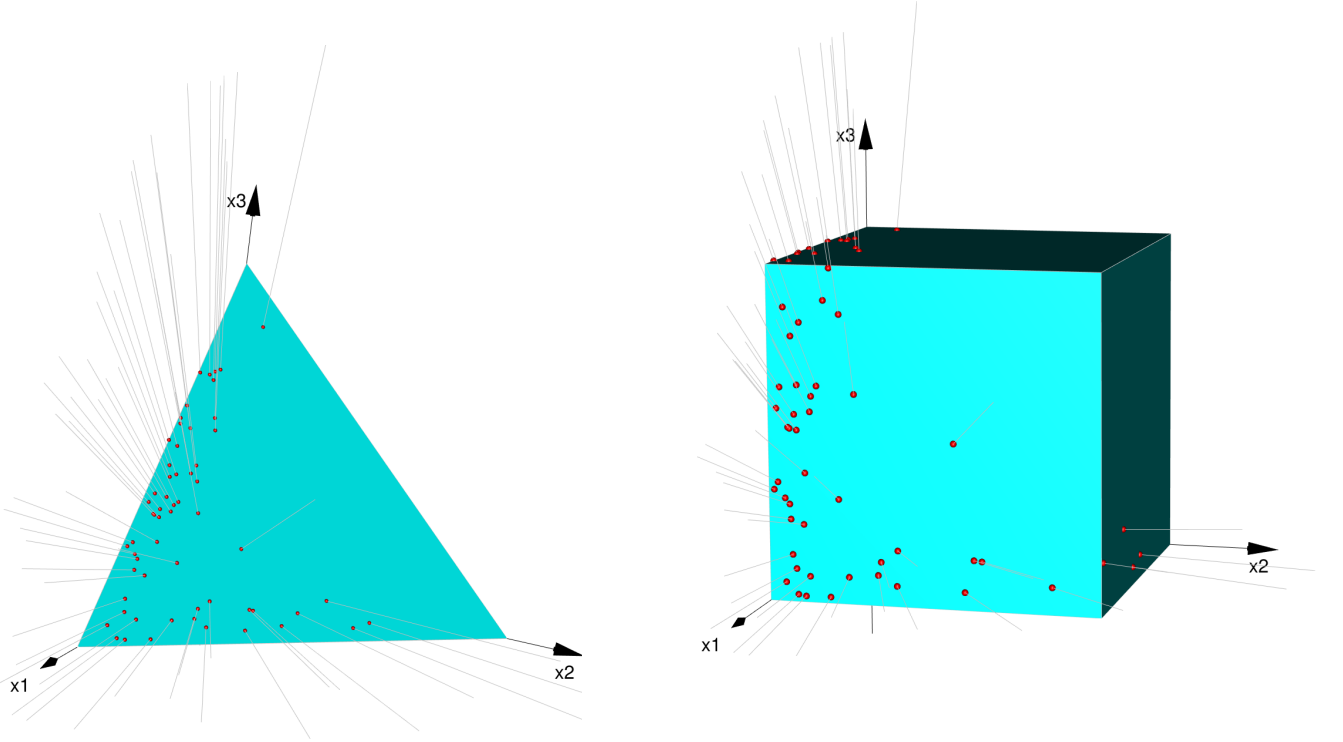


Figure 9: L^1 and L^∞ -normalizations of the data from Figure 2 of Section 2 are the projections of these points, represented as gray lines, onto the standard simplex Δ^2 for the L^1 -normalization (left) the L^∞ -simplex Δ_∞^2 for the L^∞ -normalization (right).

The L^∞ -normalization $\pi_\infty : \mathbb{R}_{\geq 0}^{d+1} - \{0\} \rightarrow \Delta_\infty^d$

$$\pi_\infty(x_0, x_1, \dots, x_d) = \frac{1}{\|x\|_\infty} (x_0, x_1, \dots, x_d)$$

is a single-component ratio transformation

$$(x_0, x_1, \dots, x_d) \mapsto \left(\frac{x_0}{x_{\text{ref}}}, \frac{x_1}{x_{\text{ref}}}, \dots, \frac{x_d}{x_{\text{ref}}} \right)$$

where x_{ref} is the maximum component value $\|x\|_\infty$. This implies that π_∞ is subcompositionally coherent with respect to all sub-setting of component operations involving components that are not maximal in any sample.

The special role of L^∞ -normalization is highlighted by Greenacre's finding, which shows that PCA analysis on data transformed using centered log ratio

$$\pi_{\text{CLR}}(x_0, x_1, \dots, x_d) = \left(\log \left(\frac{x_0}{g(x)} \right), \dots, \log \left(\frac{x_d}{g(x)} \right) \right),$$

within the interior of the standard simplex, where $g(x) = \left(\prod_{i=0}^d x_i \right)^{1/(d+1)}$ is the geometric mean of $x = (x_0, x_1, \dots, x_d)$, can be viewed as the limit of correspondence analysis (CA) on L^1 -normalized data that has undergone power transformation and rescaling [5]. The power transformation $r_p : \Delta^d \rightarrow \Delta_p^d$

$$r_p(x_0, x_1, \dots, x_d) = (x_0^{1/p}, x_1^{1/p}, \dots, x_d^{1/p})$$

is a homeomorphism between the standard simplex Δ^d and the L^p -simplex Δ_p^d for any $p \neq 2$. When compositional data are power transformed with r_p , re-scaled row-wise, and analyzed with CA, followed by rescaling the solution by p , this process converges to PCA on the CLR transformed data as p approaches ∞ . Geometrically, as p approaches ∞ , the L^p -simplex Δ_p^d converges to the L^∞ -simplex Δ_∞^d and in the limit the L^p normalization becomes L^∞ normalization.

5. L^∞ -Decomposition of Compositional Spaces

The L^∞ -simplex Δ_∞^d has a L^∞ -decomposition into $(d + 1)$ d -dimensional L^∞ -cells

$$\Delta_\infty^d = Q_0 \cup Q_1 \cup \dots \cup Q_d$$

with Q_k defined as the intersection of the L^∞ -simplex Δ_∞^d with the hyper-plane $x_k = 1$. Thus, Q_k , consists of samples where the absolute abundance of the k -th component is equal to or greater than the absolute abundances of all other components. Q_k is homeomorphic with the unit hypercube $[0, 1]^d$ as the condition $x_k = 1$ implies that the other than x_k coordinates of the L^∞ -simplex can take any value in the closed interval $[0, 1]$. Since there are d such coordinates (after excluding x_k) Q_k can be identified with the unit hypercube $[0, 1]^d$.

Since $\mathbb{RP}_{\geq 0}^d$ is homeomorphic to Δ_∞^d , the L^∞ -decomposition of Δ_∞^d into top dimensional cells induces an L^∞ -decomposition of $\mathbb{RP}_{\geq 0}^d$

$$\mathbb{RP}_{\geq 0}^d = Q_0^c \cup Q_1^c \cup \dots \cup Q_d^c$$

where Q_k^c is the set of lines through the origin in $\mathbb{R}_{\geq 0}^{d+1}$ that pass through Q_k . Thus, Q_k^c consists of compositions $[x_0 : x_1 : \dots : x_d]$, such that $x_k \geq x_i$ for all $i \neq k$. The L^∞ -decomposition of $\mathbb{RP}_{\geq 0}^d$ induces a decomposition into $d + 1$ components of any parametrization of $\mathbb{RP}_{\geq 0}^d$. In particular, the standard simplex, Δ^d , has an L^∞ -decomposition as illustrated on the following figure.

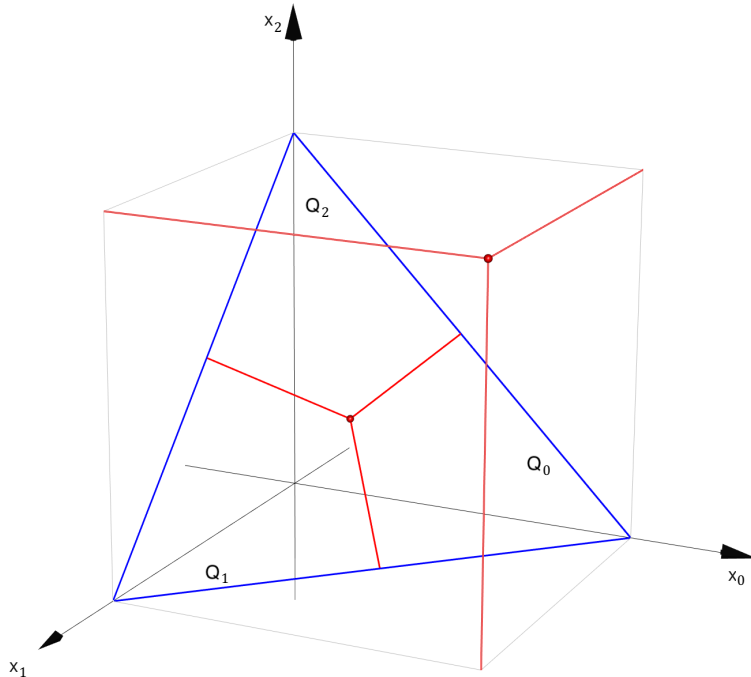


Figure 10: L^∞ -decomposition of the L^∞ and standard two-dimensional simplices.

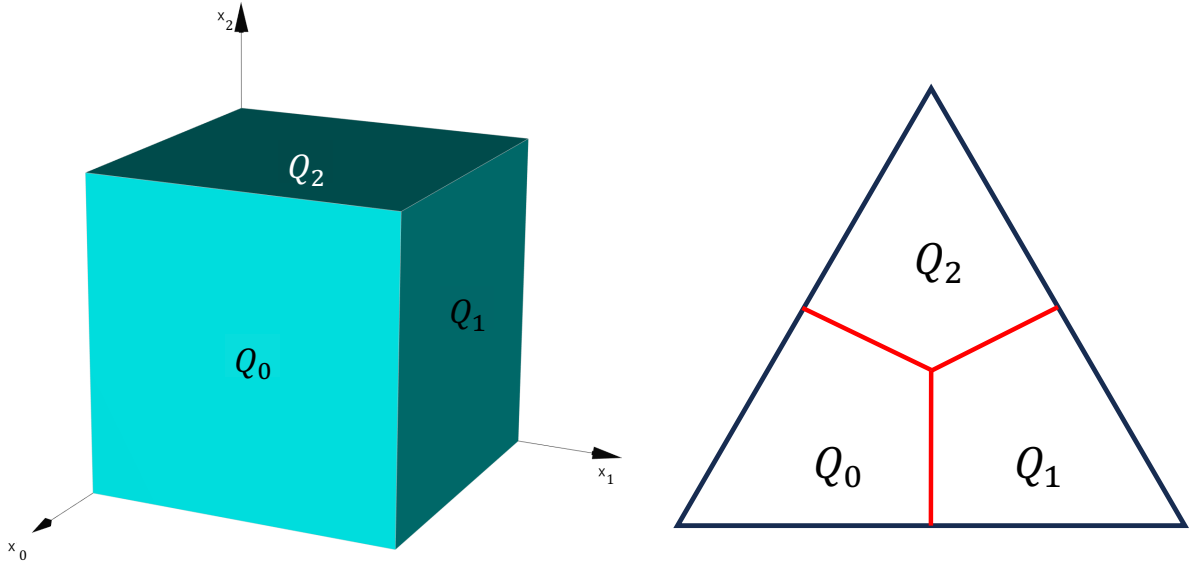


Figure 11: L^∞ -decomposition of the L^∞ and standard three-dimensional simplices.

L^∞ -decomposition of $\mathbb{RP}_{\geq 0}^d$ allows systematic study of the local structure of compositional data, by restricting attention to the subsets of data contained in different Q_k^c region of $\mathbb{RP}_{\geq 0}^d$. One may be concerned by the fact that with large number of components, a number that may be in thousands, it may be impractical to perform analyses on large number of Q_k^c cells. Typically, this is not the case as shown in Table 1 where 96.9% of 13,231 samples of the combined vaginal 16S rRNA amplicon data [3] is contained in the first 13 L^∞ -cells with the first two cells containing almost 60% of all data. The number of components in this dataset is 199.

Phylotype	Freq	Perc	CumPerc	n(det)	p(det)
<i>Lactobacillus iners</i>	4068	30.7	30.7	11884	89.8
<i>Lactobacillus crispatus</i>	3686	27.9	58.6	10605	80.2
<i>Gardnerella vaginalis</i>	2422	18.3	76.9	10272	77.6
<i>BVAB1</i>	657	5.0	81.9	5446	41.2
<i>Lactobacillus gasseri</i>	428	3.2	85.1	5980	45.2
<i>Lactobacillus jensenii</i>	414	3.1	88.2	6396	48.3
<i>Atopobium vaginae</i>	280	2.1	90.4	7520	56.8
<i>g Streptococcus</i>	250	1.9	92.2	8128	61.4
<i>Sneathia sanguinegens</i>	236	1.8	94.0	6067	45.9
<i>g Bifidobacterium</i>	178	1.3	95.4	3166	23.9
<i>g Enterococcus</i>	68	0.5	95.9	2536	19.2
<i>g Anaerococcus</i>	67	0.5	96.4	10085	76.2
<i>g Corynebacterium 1</i>	64	0.5	96.9	8677	65.6

Table 1: Frequencies, percentages and cumulative percentages of samples of the L^∞ -cells as well as the number and percentage of samples where the corresponding phylotype was detected in the combined vaginal 16S rRNA amplicon data [3].

Typically, points found in L^∞ -cells with few samples tend to be positioned at the boundaries near cells with a markedly larger sample size. This motivates that following construct of a truncated L^∞ -decomposition of a compositional dataset. Let n_0 be the minimal number of samples each L^∞ -cell is required to have. An n_0 -truncated L^∞ -decomposition of the data is constructed from the L^∞ -cells that contain at least n_0 elements in the following fashion. By reordering the components if necessary, we assume the first m L^∞ -cells, Q_0, Q_1, \dots, Q_m , contain at least n_0 elements. Any point $[x]$ from an L^∞ -cell Q_k with $k > m$ is reassigned

to the cell Q_i if the i -th component of $[x]$ has the highest value among the first m components of $[x]$.

L^∞ -decomposition can be further refined by subdividing each L^∞ -cell into 2^d equal size sub-hypercubes. This produces a very large number sub-cells. Typically, a very small subset of these holds the data. The sub-cells with small number of samples can be merged with cells carrying more samples using the truncation algorithm outlined above.

6. CSTs and L^∞ -CSTs

Community state types (CSTs) were originally defined as clusters of vaginal samples derived using hierarchical clustering with Ward linkage over a vaginal 16S rRNA amplicon data [11]. They were introduced as a tool to facilitate a high level characterization of the structure of vaginal microbial communities and have been instrumental in advancing our understanding of conditions like bacterial vaginosis and preterm delivery [13, 14, 9]. In order to remove the dependence of CST assignment on the clustering of the data a VALENCIA CST classifier was created [3].

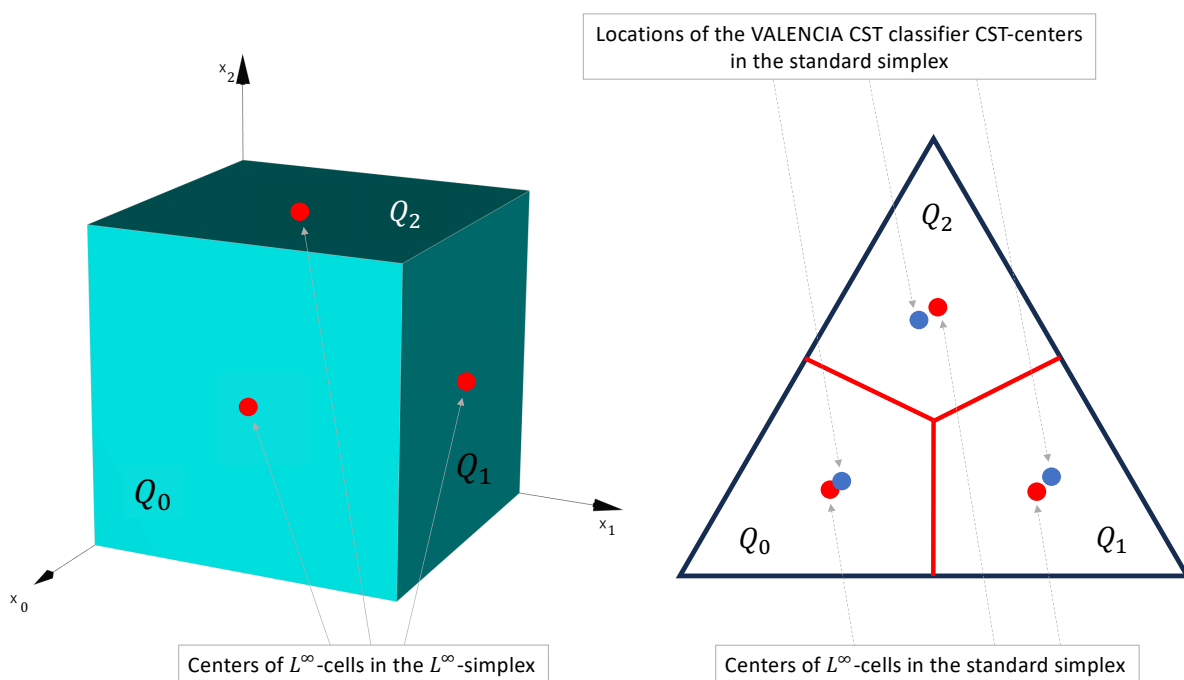


Figure 12: The mapping of L^∞ -cells from the L^∞ -simplex (left) into the standard simplex (right) maps the centers of the L^∞ -simplex cells into the centers of the corresponding regions in the standard simplex (shown as red disks). VALENCIA CST classifier uses CST centers (shown as blue disks) in the standard simplex, derived from the training dataset of large number of vaginal samples, to classify vaginal samples to CSTs. The comparison of VALENCIA CSTs and L^∞ -CSTs tables indicate that the VALENCIA CST centers are located close to the centers of the corresponding L^∞ -cells (shown in red) in the standard simplex.

The following tables compare VALENCIA CSTs with the L^∞ -cells with at least 50 samples within the dataset consisting of 13,231 vaginal samples [3] showing a high level of concordance between L^∞ -cells and VALENCIA CSTs. Thus, one can think of L^∞ -cells as an alternative construct of CSTs. This perspective shifts the understanding of CSTs and enterotypes from clusters to groupings of samples based on patterns of species dominance. Since L^∞ -cells are defined using ratios of relative abundances, that are the same as ratio of absolute abundances, L^∞ -cells define groups of samples where the absolute abundance of one species (the reference of the given cell) is at least as high or higher than the absolute abundance of other

species within the given set of samples. This approach provides clear criteria for assigning samples to CSTs or enterotypes, addressing the following limitations inherent in clustering-based approaches for constructing CSTs or enterotypes.

1) The definition of CSTs and enterotypes is highly dependent on the choice of a clustering algorithm. This has led to a situation in which distinct research groups adopt different algorithms for defining CSTs or enterotypes, making it impossible to compare their results with the results of other groups based on different definition of CSTs or enterotypes.

2) Since CSTs and enterotypes are defined using complex clustering algorithms, they don't offer clear, easily understandable criteria that determine why a sample is for example classified to CST I, effectively acting as a black box classifier.

3) The structure of the space of microbial community states is a continuum, rather than a collection of discrete, distinct clusters. Consequently, the application of clustering strategies that artificially segment this continuum is difficult to justify.

4) Clustering-based construction of CSTs and enterotypes is dataset dependent, whereas L^∞ -cell assignment is sample-dependant. Altering the dataset by adding or removing samples can shift the assignment of CSTs or enterotypes. On the other hand, an assignment to a L^∞ -cell does not depend on other samples. L^∞ -CST assignment depends on other samples only for a minority of rare samples. One solution to this CST/enterotype problem is to develop a classifier trained on the entirety of the available data [3]. However, this approach introduces a new challenge: as new data emerges, the algorithm must be updated, resulting in revised CSTs that may not align with previous versions.

The mentioned challenges significantly complicate the creation of CSTs in new microbiome contexts, where identifying meaningful clusters is inherently difficult due to the absence of clear groupings.

The use of L^∞ -cells offers a significant advantage for high-level characterization of microbiota. These cells are not just groupings of samples; they also incorporate a homogeneous coordinate system that enhances the elucidation of their internal structure. As discussed in Section 8, this coordinate system can be extended to include all samples, even those where the denominator is zero. This extension effectively maps each L^∞ -cell to a subset of a hypercube $[0, 1]^d$. This mapping facilitates a comprehensive study of the global structure of microbial community states from various perspectives.

L^∞ -cell	I	II	III	IV-A	IV-B	IV-C	V
<i>Lactobacillus iners</i>	0.0	0.0	93.1	0.7	3.6	0.3	2.3
<i>Lactobacillus crispatus</i>	98.6	0.0	1.0	0.0	0.1	0.2	0.0
<i>Gardnerella vaginalis</i>	0.2	0.7	0.4	5.9	92.5	0.1	0.3
<i>BVAB1</i>	0.0	0.0	0.0	100.0	0.0	0.0	0.0
<i>Lactobacillus gasseri</i>	0.2	99.5	0.0	0.0	0.2	0.0	0.0
<i>Lactobacillus jensenii</i>	0.5	0.0	0.0	0.0	0.0	0.5	99.0
<i>Atopobium vaginae</i>	0.4	0.0	0.7	3.2	92.5	0.4	2.9
<i>g Streptococcus</i>	0.0	0.0	0.0	0.0	0.4	99.6	0.0
<i>Sneathia sanguinegens</i>	0.0	0.0	1.3	15.7	80.9	1.7	0.4
<i>g Bifidobacterium</i>	0.0	0.0	0.0	0.0	1.1	98.9	0.0
<i>g Enterococcus</i>	0.0	0.0	0.0	0.0	0.0	100.0	0.0
<i>g Anaerococcus</i>	1.5	0.0	0.0	1.5	23.9	73.1	0.0
<i>g Corynebacterium 1</i>	1.6	3.1	0.0	0.0	1.6	93.8	0.0

Table 2: Percentages of L^∞ -cells present in different CSTs using Valencia 16S rRNA data. Only L^∞ -cells with at least 50 samples were analyzed.

L^∞ -cell	I-A	I-B	II	III-A	III-B	IV-A	IV-B	IV-C0	IV-C1	IV-C2	IV-C3	IV-C4	V
<i>Lactobacillus iners</i>	0.0	0.0	0.0	56.2	36.9	0.7	3.6	0.2	0.0	0.0	0.0	0.1	2.3
<i>Lactobacillus crispatus</i>	68.4	30.2	0.0	0.0	1.0	0.0	0.1	0.2	0.0	0.0	0.0	0.0	0.0
<i>Gardnerella vaginalis</i>	0.0	0.2	0.7	0.0	0.4	5.9	92.5	0.0	0.1	0.0	0.0	0.0	0.3
<i>BVAB1</i>	0.0	0.0	0.0	0.0	0.0	100.0	0.0	0.0	0.0	0.0	0.0	0.0	0.0
<i>Lactobacillus gasseri</i>	0.0	0.2	99.5	0.0	0.0	0.0	0.2	0.0	0.0	0.0	0.0	0.0	0.0
<i>Lactobacillus jensenii</i>	0.0	0.5	0.0	0.0	0.0	0.0	0.0	0.5	0.0	0.0	0.0	0.0	99.0
<i>Atopobium vaginae</i>	0.0	0.4	0.0	0.0	0.7	3.2	92.5	0.0	0.4	0.0	0.0	0.0	2.9
<i>g Streptococcus</i>	0.0	0.0	0.0	0.0	0.0	0.0	0.4	3.2	95.2	0.4	0.8	0.0	0.0
<i>Sneathia sanguinegens</i>	0.0	0.0	0.0	0.0	1.3	15.7	80.9	0.8	0.4	0.4	0.0	0.0	0.4
<i>g Bifidobacterium</i>	0.0	0.0	0.0	0.0	0.0	0.0	1.1	0.0	0.0	0.0	98.9	0.0	0.0
<i>g Enterococcus</i>	0.0	0.0	0.0	0.0	0.0	0.0	0.0	0.0	0.0	100.0	0.0	0.0	0.0
<i>g Anaerococcus</i>	0.0	1.5	0.0	0.0	0.0	1.5	23.9	71.6	1.5	0.0	0.0	0.0	0.0
<i>g Corynebacterium 1</i>	0.0	1.6	3.1	0.0	0.0	0.0	1.6	87.5	1.6	3.1	1.6	0.0	0.0

Table 3: Percentage of L^∞ -cells present in different sub-CSTs using Valencia 16S rRNA data. Only L^∞ -cells with at least 50 samples were analyzed.

L^∞ -cell	III	I	IV-B	IV-A	IV-C	V	II
<i>Atopobium vaginae</i>	0.1	0.0	9.1	1.0	0.2	1.5	0.0
<i>BVAB1</i>	0.0	0.0	0.0	74.9	0.0	0.0	0.0
<i>g Anaerococcus</i>	0.0	0.0	0.6	0.1	7.8	0.0	0.0
<i>g Bifidobacterium</i>	0.0	0.0	0.1	0.0	27.9	0.0	0.0
<i>g Corynebacterium 1</i>	0.0	0.0	0.0	0.0	9.5	0.0	0.4
<i>g Enterococcus</i>	0.0	0.0	0.0	0.0	10.8	0.0	0.0
<i>g Streptococcus</i>	0.0	0.0	0.0	0.0	39.5	0.0	0.0
<i>Gardnerella vaginalis</i>	0.2	0.1	78.4	16.3	0.3	1.5	3.6
<i>Lactobacillus crispatus</i>	1.0	99.7	0.1	0.1	1.4	0.2	0.0
<i>Lactobacillus gasseri</i>	0.0	0.0	0.0	0.0	0.0	0.0	95.5
<i>Lactobacillus iners</i>	98.6	0.0	5.1	3.3	1.7	17.7	0.4
<i>Lactobacillus jensenii</i>	0.0	0.1	0.0	0.0	0.3	78.8	0.0
<i>Sneathia sanguinegens</i>	0.1	0.0	6.7	4.2	0.6	0.2	0.0

Table 4: Percentage of CSTs present in different L^∞ -cells using Valencia 16S rRNA data. Only L^∞ -cells with at least 50 samples were analyzed.

Based on the notable agreement between L^∞ -cells and CSTs, we define the cells of the truncated L^∞ -decomposition, with the minimal cell size of 50 samples, as L^∞ -CSTs. In the truncated L^∞ -decomposition samples from L^∞ -cells with less than 50 samples are reassigned to those with at least 50 samples. This rearrangement is supported by the observation that samples in lesser-populated L^∞ -cells are typically situated near the boundary of that cell adjoining L^∞ -cells with a high sample count.

The mapping between L^∞ -CSTs and VALENCIA CSTs is presented in the Table 5. Each L^∞ -CST is assigned with the VALENCIA CST with the largest number of samples within that L^∞ -CST. It is important to note that none of the L^∞ -CSTs was assigned to CST I-B due to the predominant presence of CST I-B samples in the *Lactobacillus crispatus* L^∞ -CST, with the remainder scattered across L^∞ -cells holding less than 50 samples each. Additionally, three L^∞ -CSTs correspond to CST IV-B and two to CST IV-C0, thereby segmenting these CSTs into distinct groups based on their unique absolute abundance patterns.

L^∞ -CST	CST	n(comm)	n(CST)	n(L^∞ -CST)
<i>Lactobacillus crispatus</i>	I-A	2522	2522	3702
<i>Lactobacillus gasseri</i>	II	432	454	436
<i>Lactobacillus iners</i>	III-A	2288	2288	4116
<i>BVAB1</i>	IV-A	679	925	679
<i>Atopobium vaginae</i>	IV-B	283	3018	312
<i>Gardnerella vaginalis</i>	IV-B	2340	3018	2549
<i>Sneathia sanguinegens</i>	IV-B	212	3018	265
<i>g Anaerococcus</i>	IV-C0	80	210	103
<i>g Corynebacterium 1</i>	IV-C0	71	210	85
<i>g Streptococcus</i>	IV-C1	254	260	279
<i>g Enterococcus</i>	IV-C2	89	95	96
<i>g Bifidobacterium</i>	IV-C3	185	189	192
<i>Lactobacillus jensenii</i>	V	412	522	417

Table 5: Mapping of L^∞ -CSTs onto VALENCIA CSTs with the number of samples common to the corresponding CSTs (column n(comm)), the number of samples in the given VALENCIA CST (column n(CST)) and the number of samples in the corresponding L^∞ -CST (column L^∞ -CST).

Given the reduced prevalence of single-species dominance within the gut microbiome, it may be important to examine patterns where a consortium of bacteria collectively dominates a community. This shift in perspective can unveil more profound insights into the structure gut microbiome’s community state space. Consequently, this analysis requires transitioning from focusing on top-dimensional L^∞ -cells to exploring lower-dimensional L^∞ -cells defined as the intersection of several top-dimensional L^∞ -cells, offering a more nuanced view of microbial dominance.

7. Alignment of L^∞ -cells through rotation

One-dimensional L^∞ -simplex Δ_∞^1 decomposes as a union of two unit intervals $Q_0 = \{1\} \times [0, 1]$ and $Q_1 = [0, 1] \times \{1\}$ (see the left panel of Figure 13). If we rotate the L^∞ -cell Q_0 around the point $(1, 1)$, keeping the vertex $(1, 1)$ of Q_0 fixed, to the horizontal position, the image rQ_0 of Q_0 after rotation will be aligned with Q_1 , both lying on the $x_1 = 1$ line, with rQ_0 following Q_1 (see the right panel of Figure 13). The new coordinates on the rotated Q_0 are $(2 - y, 1)$, where $y \in [0, 1]$ and $Q_0 = \{(1, y) : y \in [0, 1]\}$. Thus, the rotation of Q_0 is given by the mapping. $(1, y) \mapsto (2 - y, 1)$. This, gives an explicit homeomorphism between Δ_∞^1 and the interval $[0, 2]$.

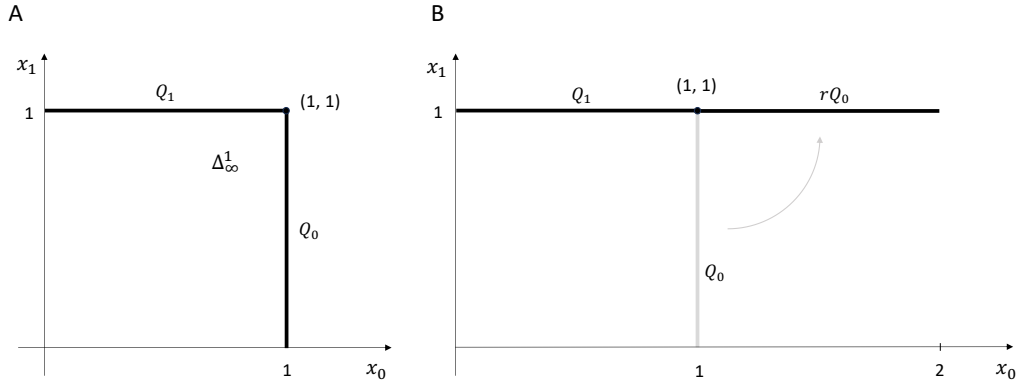


Figure 13: Rotation of the face Q_0 around the point $(1, 1)$.

The same rotation procedure can be applied to L^∞ -cells of the L^∞ -simplex in any dimension as shown in

the two-dimensional case in the following figure.

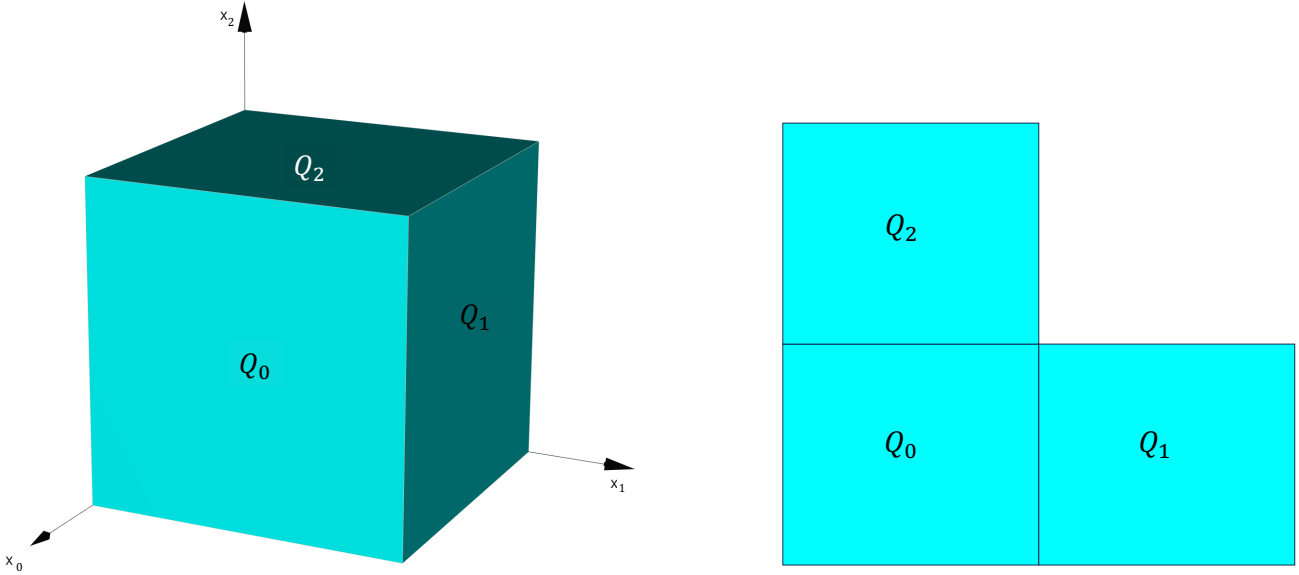


Figure 14: Unfolding the cells of Δ_∞^2 by rotation around the edges adjacent to the cell Q_0 .

The formula for the rotation of Q_j around the face common with Q_i , so that the rotated Q_j aligns with Q_i , assuming $i < j$, is

$$r_{ij}(\dots, x_i, x_{i+1}, \dots, x_{j-1}, 1, \dots) = (\dots, 1, x_{i+1}, \dots, x_{j-1}, 2 - x_i, \dots)$$

That is, the i -th coordinate in the rotated Q_j is set to 1 and the j -th coordinate is $2 - x_i$.

By stretching the L^∞ -cells adjacent to the L^∞ -cell Q_i to which the other L^∞ -cells are aligned ($Q_i = Q_0$ in Figure 14 and reshaped are L^∞ -cells Q_1 and Q_2) we get a global coordinate system $r_i : \mathbb{RP}_{\geq 0}^d \rightarrow [0, 2]^d$ over $\mathbb{RP}_{\geq 0}^d$ (see Figure 15 for the reshaping process and Figure 16 for the final result after stretching all cells adjacent to the central cell). The map though is not smooth in the interior of $\mathbb{RP}_{\geq 0}^d$ and in the next section we are going to show how one can create smooth global coordinate systems over any composition spaces.

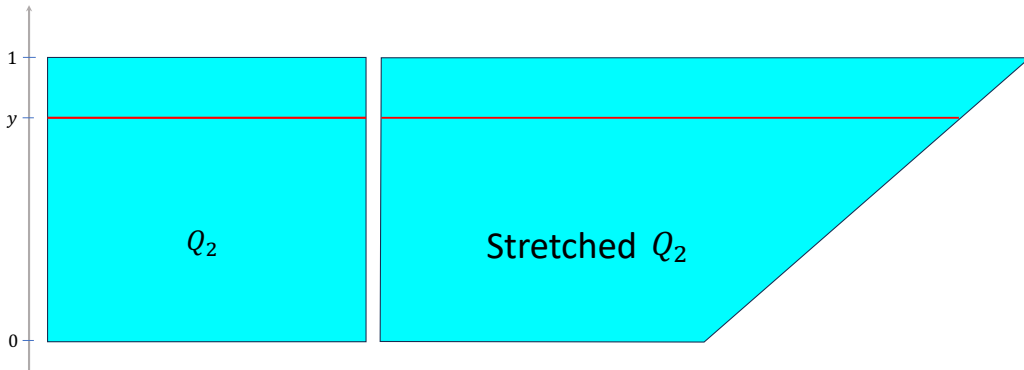


Figure 15: Reshaping the L^∞ -cell Q_2 of Δ_∞^2 so that after similar reshaping of the L^∞ -cell Q_1 the resulting regions is $[0, 2]^2$, creating a global (non-smooth) coordinate system over Δ_∞^2 . The reshaping the L^∞ -cell Q_2 sends a line interval at the height y of Q_2 into a line interval in the stretched Q_2 that is of length $1 + y$. Thus, the stretching transformations has the formula $(x, y) \mapsto ((1 + y)x, y)$ in the 2d case.

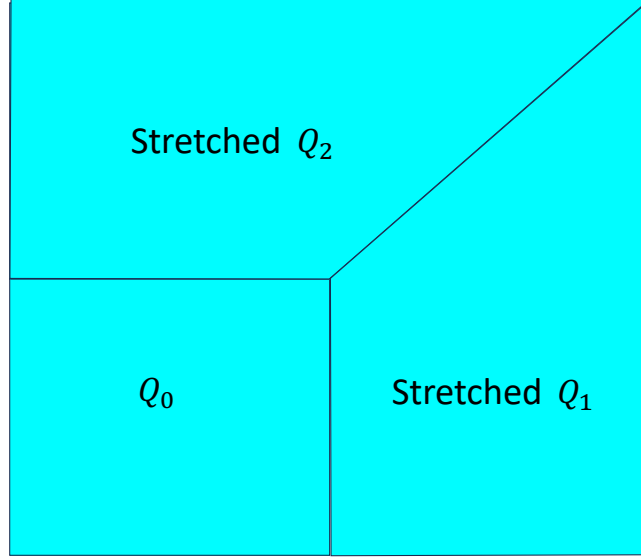


Figure 16: Reshaping the cells of Δ_∞^2 to create a global (non-smooth) coordinate system over Δ_∞^2 .

8. Hypercube Embeddings of Compositional Data

The k -th homogeneous coordinate chart, ϕ_k , induces a homeomorphism between $\mathbb{RP}_{\geq 0}^d - \{x_k = 0\}$ and $[0, \infty)^d$ as it is a restriction of the the k -th homogeneous coordinate chart homeomorphism $\mathbb{RP}_{\geq 0}^d - \{x_k = 0\} \rightarrow \mathbb{R}^d$ to $\mathbb{RP}_{\geq 0}^d$. Given that the interval $[0, \infty)$ is homeomorphic to $[0, 1)$, the product space $[0, \infty)^d$ is likewise homeomorphic to $[0, 1)^d$. Consequently, there is a mapping

$$\psi \circ \phi_k : \mathbb{RP}_{\geq 0}^d - \{x_k = 0\} \rightarrow [0, 1)^d$$

where ψ is a homeomorphism between $[0, \infty)^d$ and $[0, 1)^d$. A natural question then arises: Is it possible to find ψ such that $\psi \circ \phi_k$ extends to a homeomorphism $\hat{\phi}_k^\psi : \mathbb{RP}_{\geq 0}^d \rightarrow [0, 1]^d$, effectively providing a global coordinate system for the compositional space.

In this section, we present a simple geometric construct of a homeomorphism $r^\sigma : [0, \infty)^d \rightarrow [0, 1]^d$, such that the composition $r^\sigma \circ \phi_k$ extends to a hypercube embedding $\hat{\phi}_k^\sigma : \mathbb{RP}_{\geq 0}^d \rightarrow [0, 1]^d$. The mapping r^σ is a generalization of the sigmoidal map $\sigma : [0, \infty) \rightarrow [0, 1)$ to higher dimensions, and the construction of an extension $\hat{\phi}_k^\sigma$ is a generalization of the extension of $\sigma \circ \phi_1 : \mathbb{RP}_{\geq 0}^1 - \{x_1 = 0\} \rightarrow [0, 1)$ to $\hat{\phi}_1^\sigma : \mathbb{RP}_{\geq 0}^1 \rightarrow [0, 1]$ presented in Example 2-C of Section 2 to higher dimensions.

Before presenting a general construction of a homeomorphism $r^\sigma : [0, \infty)^d \rightarrow [0, 1]^d$, such that the composition $r^\sigma \circ \phi_k$ extends to a homeomorphism $\hat{\phi}_k^\sigma : \mathbb{RP}_{\geq 0}^d \rightarrow [0, 1]^d$, we are going to illustrate the construct in the two-dimensional case. In dimension two, the value, $\phi_1([x_0 : x_1 : x_2])$, of the 2-nd homogeneous coordinate chart ϕ_1 can be geometrically interpreted as the intersection $(\frac{x_0}{x_1}, 1, \frac{x_2}{x_1})$ of the line $\{\lambda(x_0, x_1, x_2)\}_{\lambda \in [0, \infty)}$ representing $[x_0 : x_1 : x_2]$ with the plane $x_1 = 1$ together with the identification of that plane with \mathbb{R}^2 by dropping the 1 at the second coordinate position (see Figure 17). Since we are considering the restriction of ϕ_1 to $\mathbb{RP}_{\geq 0}^d$, the line $\{\lambda(x_0, x_1, x_2)\}_{\lambda \in [0, \infty)}$ is intersected with the positive orthant $H_1 = \mathbb{R}_{\geq 0}^3 \cap \{x_1 = 1\}$ of the plane $x_1 = 1$ that is homeomorphic with $[0, \infty)^2$.

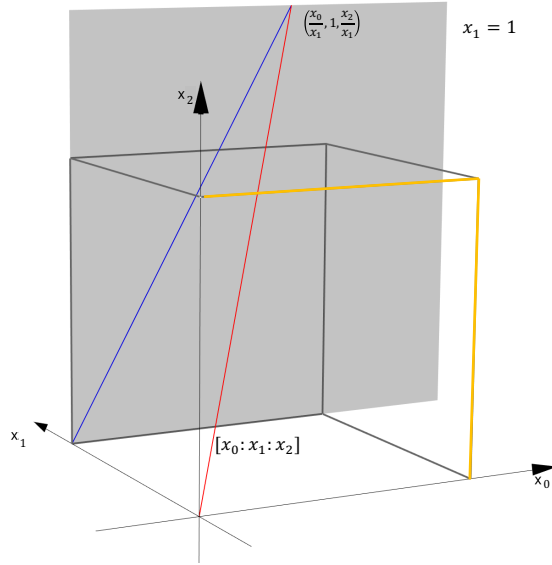


Figure 17: Geometric interpretation of ϕ_1 together with the outline of the L^∞ -simplex Δ_∞^2 with the subset $\Delta_\infty^{1,2}$ shown in orange of the points of Δ_∞^2 contained in the plane $x_1 = 0$. The shaded area is H_1 .

Consider a line that passes through the origin of the positive orthant plane H_1 and the point $(\frac{x_0}{x_1}, 1, \frac{x_2}{x_1})$, shown in Figures 17, 18, 19 in blue. The L^∞ -normalization of the line is the projection of that line on Δ_∞^2 as shown in red in Figure 18.

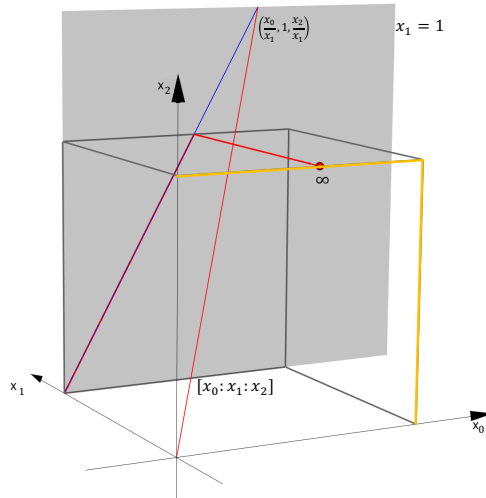


Figure 18: Projection of the line (shown in blue) through the origin of the plane $x_1 = 1$ and the point $(\frac{x_0}{x_1}, 1, \frac{x_2}{x_1})$ onto Δ_∞^2 - shown in red. Together with the point on $\Delta_\infty^{1,2} = \{x_1 = 0\} \cap \Delta_\infty^2$ shown as red sphere that is mapped to a specific point at infinity of the blue line.

This suggests a mapping of $H_1 \cong [0, \infty)^2$ onto $[0, 1]^2$, interpreted as a subset of the unit square of the plane $x_1 = 0$, that sends any line (shown in blue) through the origin in H_1 onto the open line segment (shown in red in Figure 19) corresponding to that line within the unit L^∞ -disk in the plane $x_1 = 0$, defined as the set $\{(x_0, 0, x_2) : 0 \leq x_i \leq 1, \}$. The mapping is given by the radial- σ map r^σ that maps $z \in [0, \infty)^2$ into $\sigma(\|z\|_1) \frac{z}{\|z\|_\infty} \in [0, 1]^2$ (see Figure 19). In general, the radial- σ map r^σ maps $z \in [0, \infty)^d$ into $\sigma(\|z\|_1) \frac{z}{\|z\|_\infty} \in [0, 1]^d$.

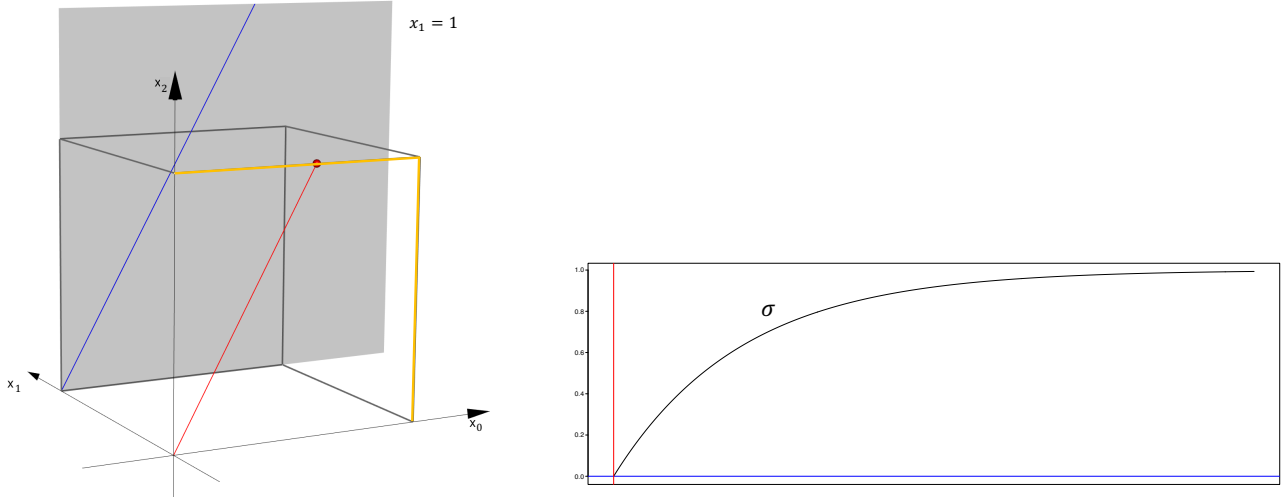


Figure 19: Any line through the origin in H_1 , shown in blue, is sent by radial- σ to the fragment of the same line (after parallel shift from the $x_1 = 1$ plane to the $x_1 = 0$ plane) restricted to the open unit square $[0, 1]^2$.

In general, the composition $\phi_k^\sigma = r^\sigma \circ \phi_k$ is defined for $[x]$ in $\mathbb{RP}_{\geq 0}^d - \{x_k = 0\}$ as

$$\phi_k^\sigma([x]) = \sigma(\|\phi_k([x])\|_1) \frac{\phi_k([x])}{\|\phi_k([x])\|_\infty}$$

The extension $\hat{\phi}_k^\sigma$ of ϕ_k^σ to the points of $\mathbb{RP}_{\geq 0}^d$ contained in $\{x_k = 0\}$ is defined as

$$\hat{\phi}_k^\sigma([x]) = \frac{x}{\|x\|_\infty}$$

Thus, it is the L^∞ -parametrization of the points of $\{x_k = 0\}$. When working with the L^∞ -normalized data, $\hat{\phi}_k^\sigma$ is the identity mapping over $\{x_k = 0\}$.

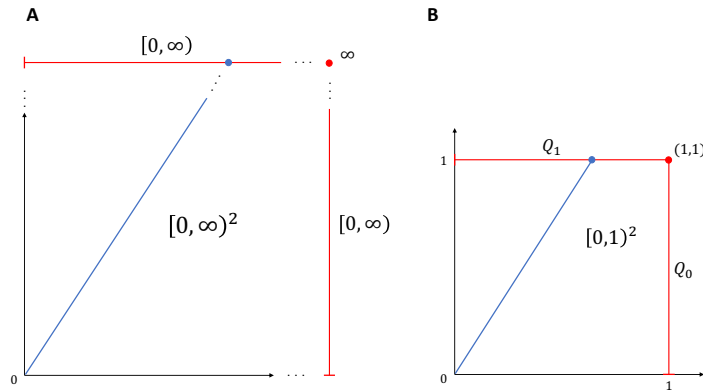


Figure 20: Extension of the radial- σ mapping from $[0, \infty)^2 \rightarrow [0, 1]^2$ to $[0, \infty)^{2*} \rightarrow [0, 1]^2$, where $[0, \infty)^{2*}$ is the compactification of $[0, \infty)^2$ with the union $[0, \infty) \cup \{\infty\} \cup [0, \infty)$, highlighted in red in Panel A. Panel B shows the unit square $[0, 1]^2$ as a compactification of $[0, 1]^2$ with $\Delta_\infty^1 = Q_0 \cup Q_1$ marked in red. The extension \hat{r}^σ maps the infinity points of the compactification $[0, \infty)^{2*}$ of $[0, \infty)^2$ through a sigmoidal function onto Δ_∞^1 . The radial- σ mapping sends the blue line in the panel A into the corresponding blue line segment in the panel B, mapping the infinite point on the left (shown as a blue disk) into the corresponding blue disk at the end of the corresponding line segment.

In the two-dimensional case, the hypercube embedding $\hat{\phi}_k^\sigma : \mathbb{RP}_{\geq 0}^2 \rightarrow [0, 1]^2$ factors out into the composition

$$\hat{r}^\sigma \circ \phi_k^* : \mathbb{RP}_{\geq 0}^2 \rightarrow [0, \infty)^{2*} \rightarrow [0, 1]^2,$$

where

$$[0, \infty)^{2*} = [0, \infty)^2 \cup [0, \infty) \cup \{\infty\} \cup [0, \infty)$$

is a compactification of $[0, \infty)^2$ depicted in the panel A of Figure 20 and \hat{r}^σ is an extension of the radial- σ mapping r^σ to a homeomorphism $[0, \infty)^{2*} \rightarrow [0, 1]^2$ mapping the first copy of $[0, \infty)$ in the compactification of $[0, \infty)^2$ to $[0, 1) \subset Q_0$ of Δ_∞^1 , mapping ∞ to $(1, 1) \in \Delta_\infty^1$ and mapping the second copy of $[0, \infty)$ in the compactification of $[0, \infty)^2$ to $[0, 1) \subset Q_1$ of Δ_∞^1 as illustrated in Figure 20. For $k = 2$, ϕ_1^* is defined over $\{x_1 = 0\}$ as

$$\phi_1^*([x_0 : 0 : x_2]) = \begin{cases} \sigma^{-1}\left(\frac{x_0}{x_2}\right) & \text{if } x_0 < x_2, \\ \infty & \text{if } x_0 = x_2, \\ \sigma^{-1}\left(\frac{x_2}{x_0}\right) & \text{if } x_0 > x_2. \end{cases}$$

In general, one can show that the hypercube embedding $\hat{\phi}_k^\sigma : \mathbb{RP}_{\geq 0}^d \rightarrow [0, 1]^d$ can be represented as the composition $\hat{r}^\sigma \circ \phi_k^* : \mathbb{RP}_{\geq 0}^d \rightarrow [0, \infty)^{d*} \rightarrow [0, 1]^d$, where $[0, \infty)^{d*}$ is a compactification of $[0, \infty)^d$ by a set of points at infinity homeomorphic to Δ_∞^{d-1} and \hat{r}^σ is an extension of the radial- σ mapping r^σ to a homeomorphism $[0, \infty)^{d*} \rightarrow [0, 1]^d$. Given that this fact is purely of theoretical nature without practical implications for analyzing real-world data, we offer the proof of this statement as a challenge to readers with a penchant for topology.

Implementing the hypercube embedding algorithm necessitates careful management of rounding errors. To address this, we employ the sigmoidal function $\sigma(x, \lambda) = 1 - e^{-\lambda x}$, and for any given dataset, we determine a value for $\lambda > 0$ that ensures $1 - e^{-\lambda M} \neq 1$ and $1 - e^{-\lambda m} \neq 0$, where M represents the maximum and m the minimum of $\|\phi_k([x])\|_1$ across the dataset. Specifically, we aim for $1 - e^{-\lambda M} < C\varepsilon$ and $1 - e^{-\lambda m} > C\varepsilon$, with ε being the smallest double floating-point number for which $1 + \varepsilon \neq 1$, and $C > 0$ fulfilling the condition:

$$-\frac{\log(C\varepsilon)}{M} \leq -\frac{\log(1 - C\varepsilon)}{m}.$$

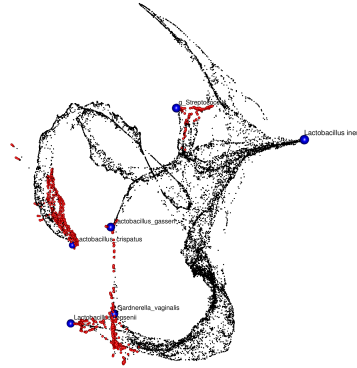


Figure 21: Low dimensional PaCMAP representation of the Li-hypercube embedding of the VALENCIA 16S rRNA dataset. The points at infinity are shown in red.

Figures 21, 22 and 23 show PaCMAP 3d representation of the Li, Lc and Gv, respectively, hypercube embeddings of the VALENCIA 16S rRNA dataset with the points at infinity shown in red. The points at infinity are smoothly adjacent to the finite points indicating the continuous nature of the hypercube embedding.

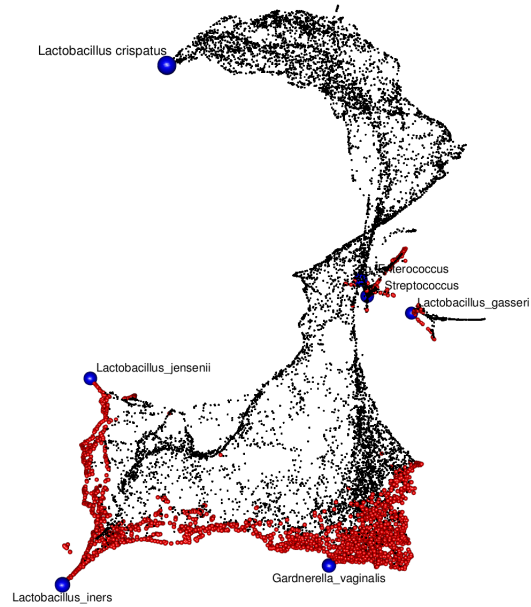


Figure 22: Low dimensional PaCMAP representation of the Lc-hypercube embedding of the VALENCIA 16S rRNA dataset.

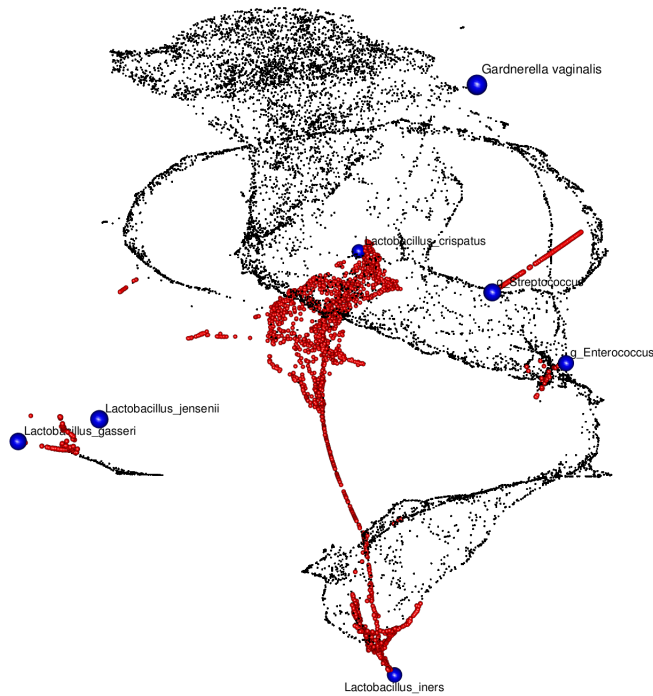


Figure 23: Low dimensional PaCMAP representation of the Gv-hypercube embedding of the VALENCIA 16S rRNA dataset.

9. Combining Cube Embeddings

Cube embeddings allow for study microbial communities from the point of view of absolute abundance ratios of all components with respect to the given reference component. Thus, for a given reference component, the cube embedding of this reference component carries information about the way abundances of other components relate with the abundance of the reference over all samples. However, the abundance of representations introduces complexity, prompting the question: Can these diverse representations be integrated? A unified representation can be defined as the Cartesian product of the cube embeddings of the data's L^∞ -CSTs or a subset of L^∞ -CSTs. The following figure shows the PaCMAP 3d representation of the product embedding of the combined Li, Lc and Gv-cube embeddings as they correspond to the largest L^∞ -CSTs.

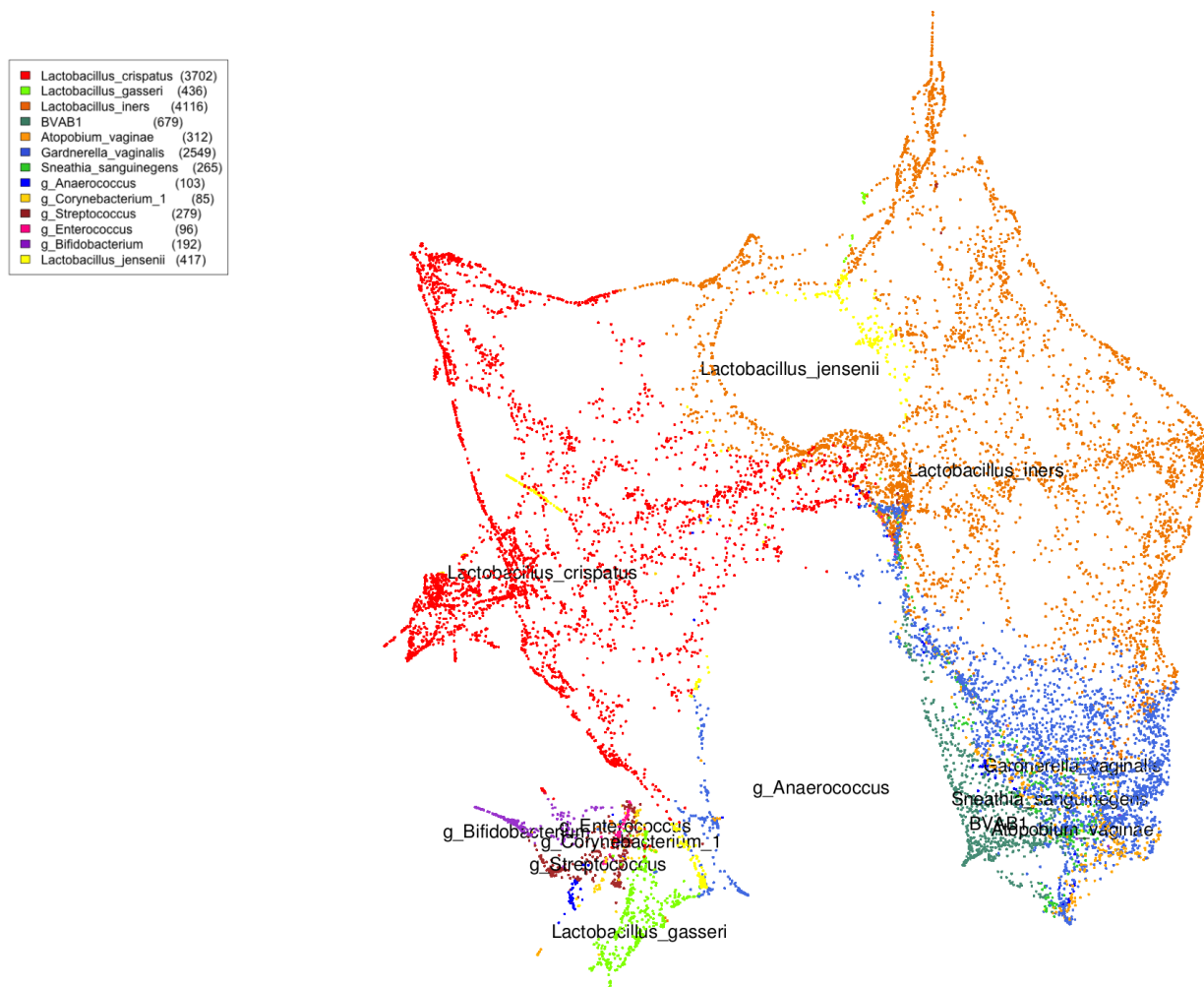


Figure 24: PaCMAP 3d embedding of the combined Li, Lc and Gv-cube embeddings color coded by L^∞ -CSTs over the VALENCIA 16S rRNA data.

10. Discussion

In this paper, we have introduced a novel approach to compositional data analysis based on L^∞ -normalization and its associated decomposition of the compositional space into L^∞ -cells. This approach addresses the challenges posed by the prevalence of zeros in high-throughput omics datasets, which are inherently compositional. By focusing on L^∞ -normalization, we have shown that it possesses advantageous properties,

such as subcompositional coherence with respect to the elimination of low-abundance components, which is particularly relevant for omics data.

The L^∞ -decomposition of the compositional space provides a new perspective on the characterization of microbial communities. We have introduced the concept of L^∞ -CSTs, which are derived from the truncated L^∞ -decomposition and offer several advantages over classical CSTs or enterotypes. These advantages include a clear and biologically meaningful definition, stability under the addition or subtraction of samples, and the provision of a homogeneous coordinate system for each L^∞ -cell, facilitating the elucidation of its internal structure. The comparison of L^∞ -CSTs with VALENCIA CSTs in the context of vaginal microbiome data has demonstrated a high level of concordance, validating the potential of L^∞ -CSTs as an alternative approach for high-level characterization of microbial communities.

While CST-like constructs provide a means for conducting CST-based association analyses, allowing for the comparison of the prevalence of different factors across distinct regions within the community state space, the segmentation of this space into CSTs can also be viewed as a limitation. This discretization of a naturally continuous state space that lacks distinct clusters can be mitigated by interpreting each L^∞ -cell as an element of a filtration $\{Q(r)\}_{r \in [0,1]}$ of a d -dimensional cube $[0, 1]^d$, where $Q(r)$ is the L^∞ -disk of radius r centered at the origin of $[0, 1]^d$. This approach allows for the analysis of the dependence of the mean prevalence of specific factors along the boundary $\partial Q(r)$ of $Q(r)$ on r . Furthermore, by identifying clusters of the given data within each $\partial Q(r)$ and representing the prevalence of specific factors along the boundary $\partial Q(r)$ of $Q(r)$ as a mixture of the components corresponding to these clusters, one can study how these mixture components depend on the distance from the origin of $[0, 1]^d$, which corresponds to the community state completely dominated by the reference component. This analytical setup can be thought of as a special case of a more general Reeb complex construct, with $\partial Q(r)$ viewed as the level sets of the L^∞ -distance from the origin function [12]. The development of these ideas is left for future research.

Furthermore, we have introduced cube embeddings, which extend homogeneous coordinates to the entire sample space, allowing for the study of compositional data from multiple perspectives. By integrating cube embeddings associated with L^∞ -CSTs, we have shown that a unified representation of the data can be obtained, providing a comprehensive understanding of the compositional data's structure.

The methods presented in this paper have broad applicability beyond microbiome studies and can be applied to any type of compositional data. The geometric and topological ideas employed in the development of these methods provide a solid foundation for further advancements in compositional data analysis.

However, there are still several aspects that require further investigation. One area of interest is the exploration of lower-dimensional L^∞ -cells, which may reveal patterns of dominance by consortia of bacteria, particularly in the context of the gut microbiome. Another avenue for future research is the application of these methods to other omics data types, such as metagenomics and metabolomics, to assess their performance and potential for uncovering novel insights.

In conclusion, the L^∞ -normalization approach and its associated methods presented in this paper offer a promising framework for compositional data analysis, particularly in the context of high-throughput omics datasets. The advantages of L^∞ -CSTs, the introduction of cube embeddings, and the integration of multiple perspectives through the Cartesian product of cube embeddings provide a comprehensive set of tools for understanding the structure of compositional data. Further research and application of these methods to diverse datasets will help to refine and extend their utility in various fields of study.

References

- [1] John Aitchison. The statistical analysis of compositional data. *Journal of the Royal Statistical Society: Series B (Methodological)*, 44(2):139–160, 1982.
- [2] John Aitchison. *The Statistical Analysis of Compositional Data*. Chapman & Hall, Ltd., GBR, 1986.

- [3] Michael France, Bing Ma, Pawel Gajer, Sarah Brown, Mike S Humphrys, Johanna B Holm, Rebecca M Brotman, and Jacques Ravel. VALENCIA: A nearest centroid classification method for vaginal microbial communities based on composition. *Microbiome*, 8(166), 2020.
- [4] Xiaoyin Ge, Issam Safa, Mikhail Belkin, and Yusu Wang. Data skeletonization via reeb graphs. *Advances in neural information processing systems*, 24, 2011.
- [5] Michael Greenacre. Power transformations in correspondence analysis. *Computational Statistics & Data Analysis*, 53(8):3107–3116, 2009.
- [6] Victor Guillemin and Alan Pollack. *Differential topology*, volume 370. American Mathematical Soc., 2010.
- [7] Bert Mendelson. *Introduction to topology*. Courier Corporation, 1990.
- [8] August Ferdinand MObius. *Der barycentrische Calcul ein neues Hilfsmittel zur analytischen Behandlung der Geometrie dargestellt und insbesondere auf die Bildung neuer Classen von Aufgaben und die Entwicklung mehrerer Eigenschaften der Kegelschnitte angewendet von August Ferdinand Mobius Professor der Astronomie zu Leipzig*. Verlag von Johann Ambrosius Barth, 1827.
- [9] D Elizabeth O’Hanlon, Pawel Gajer, Rebecca M Brotman, and Jacques Ravel. Asymptomatic bacterial vaginosis is associated with depletion of mature superficial cells shed from the vaginal epithelium. *Frontiers in cellular and infection microbiology*, 10:106, 2020.
- [10] Barrett O’neill. *Elementary differential geometry*. Elsevier, 2006.
- [11] Jacques Ravel, Pawel Gajer, Zaid Abdo, G Maria Schneider, Sara SK Koenig, Stacey L McCulle, Shara Karlebach, Reshma Gorle, Jennifer Russell, Carol O Tacket, et al. Vaginal microbiome of reproductive-age women. *Proceedings of the National Academy of Sciences*, 108(supplement_1):4680–4687, 2011.
- [12] Georges Reeb. On the singular points of a completely integrable pfaff form or of a numerical function]. *Comptes Rendus Acad. Sciences Paris*, 222:847–849, 1946.
- [13] Roberto Romero, Sonia S Hassan, Pawel Gajer, Adi L Tarca, Douglas W Fadrosch, Janine Bieda, Piya Chaemsaitong, Jezid Miranda, Tinnakorn Chaiworapongsa, and Jacques Ravel. The vaginal microbiota of pregnant women who subsequently have spontaneous preterm labor and delivery and those with a normal delivery at term. *Microbiome*, 2:1–15, 2014.
- [14] Susan Tuddenham, Khalil G Ghanem, Laura E Caulfield, Alisha J Rovner, Courtney Robinson, Rupak Shivakoti, Ryan Miller, Anne Burke, Catherine Murphy, Jacques Ravel, et al. Associations between dietary micronutrient intake and molecular-bacterial vaginosis. *Reproductive health*, 16(1):1–8, 2019.